

*promoting access to White Rose research papers*



**Universities of Leeds, Sheffield and York**  
**<http://eprints.whiterose.ac.uk/>**

---

This is an author produced version of a paper published in **Physics of Plasmas**.

White Rose Research Online URL for this paper:

<http://eprints.whiterose.ac.uk/10827>

---

**Published paper**

Li, Y. (2010) *Geometrical statistics and vortex structures in helical and nonhelical turbulences*, Physics of Plasmas, 22 (3), Article no. 035101

<http://dx.doi.org/10.1063/1.3336012>

---

# Geometrical statistics and vortex structures in helical and non-helical turbulence

Yi Li

*Department of Applied Mathematics, School of mathematics and statistics,  
University of Sheffield, Sheffield, UK, S3 7RH*

(Dated: November 30, 2009)

In this paper we conduct an analysis of the geometrical and vortical statistics in the small scales of helical and non-helical turbulence generated with direct numerical simulations. Using a filtering approach, the helicity flux from large scales to small scales is represented by the subgrid-scale (SGS) helicity dissipation. The SGS helicity dissipation is proportional to the product between the SGS stress tensor and the symmetric part of the filtered vorticity gradient, a tensor we refer to as the vorticity strain rate. We document the statistics of the vorticity strain rate, the vorticity gradient, and the dual vector corresponding to the anti-symmetric part of the vorticity gradient. These results provide new insights into the local structures of the vorticity field. We also study the relations between these quantities and vorticity, SGS helicity dissipation, SGS stress tensor, and other quantities. We observe that in both helical and non-helical turbulence: (1) there is a high probability to find the dual vector aligned with the intermediate eigenvector of the vorticity strain rate tensor; (2) vorticity tends to make an angle of 45 degrees with both the most contractive and the most extensive eigen-directions of the vorticity strain rate tensor; (3) the vorticity strain rate shows a preferred alignment configuration with the SGS stress tensor; (4) in regions with strong straining of the vortex lines, there is a negative correlation between the third order invariant of the vorticity gradient tensor and SGS helicity dissipation fluctuations. The correlation is qualitatively explained in terms of the self-induced motions of local vortex structures, which tend to wind up the vortex lines and generate SGS helicity dissipation. In helical turbulence, we observe that the joint probability density function of the second and third tensor invariants of the vorticity gradient displays skewed distributions, with the direction of skewness depending on the sign of helicity input. We also observe that the intermediate eigenvalue of the vorticity strain rate tensor is more probable to take negative values. These interesting observations, reported for the first time, call for further studies into their dynamical origins and implications.

## I. INTRODUCTION

Helicity is the scalar product between velocity and vorticity, integrated over the space. It is an invariant of the Euler equations [1–3]. It measures the alignment between velocity and vorticity and is related to the magnitude of the nonlinear term in the Navier-Stokes (NS) equations [4, 5]. Geometrically it characterizes the knottedness of vortex lines [1, 6, 7]. In turbulence with non-zero mean helicity, namely helical turbulence, it has been observed that helicity cascades from the input scales to small scales and a Kolmogorov-type helicity spectrum in the inertial range is generated [8–11]. Various aspects of helical turbulence have been studied. Examples include the geometrical properties [12], the details of helicity cascade [9–11, 13–15], the effects of helicity on energy cascade [16], the interaction between helicity and energy dissipation [17, 18], intermittency in helicity cascade [19], the correlation between helicity and enstrophy fluctuation [20], etc. Helicity plays an important role in the dynamo theory of magnetohydrodynamical flows [6, 21]. Its effects in geophysical flows are observed in [22, 23]. The combined effects of rotation and helicity are investigated in [24]. The roles of helicity in the formation of turbulence are studied in [25, 26]. The implication of helicity on the regularity of Euler equations and Navier-Stokes equations is also a subject of recent research [27–30]. For a review on various aspects of helicity and its implications, see [21].

Helicity cascade can be studied with a filtering approach [11, 31], an approach that forms the basis of large eddy simulation (LES) (see, e.g., [32] for a review of LES and related issues). In this formalism, the helicity flux from large scales to small scales is represented as the subgrid-scale (SGS) helicity dissipation rate. By deriving the equation of the resolved helicity (see Section II), it can be shown that the SGS helicity dissipation rate is given as [11]:

$$\Pi_H \equiv -2\tilde{R}_{ij}\tau_{ij} \quad (1)$$

where  $\tau_{ij} \equiv \widetilde{u_i u_j} - \tilde{u}_i \tilde{u}_j$  is the SGS stress tensor, with the tilde representing filtered quantities and  $u_i$  being the velocity.  $\tilde{R}_{ij} \equiv (\partial_i \tilde{\omega}_j + \partial_j \tilde{\omega}_i)/2$  is the symmetric part of the gradient of the filtered vorticity  $\tilde{\boldsymbol{\omega}} \equiv \nabla \times \tilde{\mathbf{u}}$ . According to Eq. (1), the SGS helicity dissipation is the product of tensors  $\tilde{R}_{ij}$  and  $\tau_{ij}$ . It shows that the local structure of the vorticity field, represented by  $\tilde{R}_{ij}$ , has close relation with the rate of helicity transfer across scales. The magnitudes of  $\tilde{R}_{ij}$  and  $\tau_{ij}$ , as well as their relative alignment, determine the value of SGS helicity dissipation.

The relative alignment between the tensors is defined in terms of their eigenvectors. Therefore, an analysis of their eigenvectors and eigenvalues is expected to be useful in revealing the mechanisms of SGS helicity dissipation. In the related problem of energy cascade, such

a geometrical point of view has proven valuable. The energy flux from large scales to small scales can be represented by the SGS energy dissipation (see, e.g., [32]):

$$\Pi_E \equiv -\tilde{S}_{ij}\tau_{ij}, \quad (2)$$

where  $\tilde{S}_{ij} \equiv (\partial_j \tilde{u}_i + \partial_i \tilde{u}_j)/2$  is the filtered strain rate tensor. Thus, the value of  $\Pi_E$  is controlled by the alignment between  $\tilde{S}_{ij}$  and  $\tau_{ij}$ . Analyses of the latter have been conducted in [33, 34], which provide not only useful information for model development, but also considerable insight into the mechanisms of SGS energy dissipation and the evolution of vortical structures. More generally, people have also looked into other geometrical statistics, such as the alignment between the strain rate tensor  $\tilde{S}_{ij}$ , vorticity  $\tilde{\omega}$ , passive scalar gradient, pressure Hessian etc [35–44]. Among others, these statistics have implications on understanding the regularity of the Euler and the NS equations (see, e.g., [45–47]). In helical turbulence, however, an analysis based on a geometrical point of view is still lacking.

Furthermore, statistics of  $\tilde{R}_{ij}$  carry useful information of the local structures of the vorticity field, which is of interests in both helical and non-helical turbulence. Related quantities, such as the gradient of vorticity, have appeared in several situations. In 2D turbulence, the gradient of vorticity controls the direct enstrophy cascade [48]. [49] shows that the spatial gradient of the direction of vorticity is intimately related to the regularity of the NS equations. The gradient of the direction of vorticity is analyzed theoretically and numerically in [50, 51]. Therefore, one expects that an analysis of  $\tilde{R}_{ij}$  and related quantities will also be beneficial.

Given the potential effects of helicity, a better understanding of the mechanisms of SGS helicity dissipation is desirable, in order to facilitate the modeling of helical turbulent flows. The knowledge of the geometry of helical turbulence also has wider implications, especially when interactions with other physical processes are involved. Thus, in this paper we adopt a filtering approach and present a geometrical analysis of helical turbulence. The purpose is three-fold. First, we aim at identifying the unique geometrical features of helical turbulence. To this end, we contrast the statistics obtained in helical turbulence with non-helical turbulence, even though some statistics (the mean SGS helicity dissipation, for example) are not particularly relevant in non-helical turbulence. Also, in addition to  $\tilde{R}_{ij}$ , we search for the signature of helicity in the gradient of vorticity and other quantities. Second, we look to elucidate the dynamical mechanisms of helicity cascade, by examining the relation between local vortical structures and SGS helicity dissipation rate. Third, we intend to document some of the statistics characterizing the gradient of vorticity, which are useful for both helical and non-helical turbulence, as explained above. For this reason, apart from the statistics mentioned above, we also consider the dual vector corresponding to the anti-

symmetric part of the vorticity gradient, its alignment with  $\tilde{R}_{ij}$ , as well as the alignment between the vorticity and  $\tilde{R}_{ij}$  etc.

The paper is organized as follows. In section 2, the definitions, basic theories, and the numerical simulations are summarized. The analysis of DNS data is presented in section 3. Conclusions are summarized in section 4.

## II. BASIC THEORIES

We use  $u_i(\mathbf{x}, t)$  to denote the  $i$ th component of the velocity vector  $\mathbf{u}(\mathbf{x}, t)$ .  $\boldsymbol{\omega}(\mathbf{x}, t) = \nabla \times \mathbf{u}$  is the vorticity vector. We consider the helicity density, defined as  $h(\mathbf{x}, t) \equiv \mathbf{u} \cdot \boldsymbol{\omega} = u_i \omega_i$ . As is conjectured in [8] and observed in simulations [10, 11], in the inertial range of helical turbulence, a  $-5/3$  helicity spectrum is established:

$$H(k) = c_H \epsilon_H \epsilon^{-1/3} k^{-5/3} \quad (3)$$

in which

$$H(k) \equiv \sum_{k \leq |\mathbf{k}| \leq k+1} \hat{\mathbf{u}}^*(\mathbf{k}) \cdot \hat{\boldsymbol{\omega}}(\mathbf{k}) \quad (4)$$

is the helicity spectrum, and  $\hat{\mathbf{u}}$  and  $\hat{\boldsymbol{\omega}}$  are, respectively, the Fourier transforms of velocity and vorticity.  $\epsilon_H$  is the helicity dissipation rate,  $\epsilon$  the energy dissipation rate, and  $c_H$  a constant found numerically to be about 1.0 [10, 52]. The helicity spectrum is established through a helicity cascade process, which has been studied in [10, 11] using DNS data.

To investigate the interscale interactions, we use a filtering approach [11, 32]. Given a filter kernel  $G_\Delta(\mathbf{r})$  with length scale  $\Delta$ , the filtered velocity  $\tilde{\mathbf{u}}$  is defined as the convolution between the filter kernel and the velocity  $\mathbf{u}$ , i.e.,

$$\tilde{\mathbf{u}}(\mathbf{x}, t) \equiv \int G_\Delta(\mathbf{r}) \mathbf{u}(\mathbf{x} + \mathbf{r}, t) d^3 \mathbf{r}. \quad (5)$$

Correspondingly, the filtered vorticity is defined as  $\tilde{\boldsymbol{\omega}} = \nabla \times \tilde{\mathbf{u}}$ , as mentioned in Section I. We then define the resolved helicity density as  $h_\Delta(\mathbf{x}, t) = \tilde{\mathbf{u}} \cdot \tilde{\boldsymbol{\omega}}$ .

From the NS equations, it is not difficult to derive the equation for  $h_\Delta$ . The filtered NS equations read:

$$D_t \tilde{u}_i = -\partial_i \tilde{p} + \partial_j (-\tau_{ij}) + \nu \nabla^2 \tilde{u}_i + \tilde{f}_i, \quad (6)$$

where  $D_t \equiv \partial_t + \tilde{u}_k \partial_k$  is the Lagrangian derivative following the filtered velocity.  $\tau_{ij}$  is the SGS stress, already given in section I.  $\tilde{p}$  is the filtered pressure (divided by density).  $\nu$  is the kinematic viscosity, and  $\tilde{f}_i$  is the filtered forcing term. As the trace of  $\tau_{ij}$  can always be absorbed into a suitably defined modified pressure, we will assume  $\tau_{ij}$  is traceless. Or

equivalently  $\tau_{ij}$  will represent the anisotropic part of the SGS stress tensor. Taking the curl of the above equation, one finds the equation for the filtered vorticity  $\tilde{\omega}$ . To simplify notations, we denote the SGS force  $-\partial_j\tau_{ij}$  by  $T_i$ . Thus the equation for  $\tilde{\omega}$  can be written as:

$$D_t\tilde{\omega} = \tilde{\mathbf{S}}\tilde{\omega} + \nabla \times \mathbf{T} + \nu\partial^2\tilde{\omega} + \nabla \times \tilde{\mathbf{f}}. \quad (7)$$

The equation for  $h_\Delta$ , after some algebra, can then be derived as follows:

$$D_t h_\Delta = \partial_j \tilde{Q}_j - \Pi_H - 4\nu \tilde{S}_{ij} \tilde{R}_{ij} + 2\tilde{f}_i \tilde{\omega}_i. \quad (8)$$

As defined in Eq. (1),  $\Pi_H \equiv -2\tau_{ij}\tilde{R}_{ij}$  on the right-hand side (RHS) of the equation is the SGS helicity dissipation rate.  $\tilde{Q}_j$  is the spatial flux vector, with its expression shown as follows:

$$\begin{aligned} \tilde{Q}_j \equiv & -2\tilde{\omega}_i \tau_{ij} - \epsilon_{ijk} \tilde{u}_i \partial_l \tau_{kl} - \tilde{\omega}_j \frac{\tilde{p}}{\rho} + \tilde{\omega}_j \frac{\tilde{u}_i \tilde{u}_i}{2} \\ & + 2\nu \tilde{R}_{ij} \tilde{u}_i + 2\nu \tilde{S}_{ij} \tilde{\omega}_i - \epsilon_{jkm} \tilde{u}_k \tilde{f}_m. \end{aligned} \quad (9)$$

In Eq. (8), the SGS helicity dissipation  $\Pi_H$  represents the helicity flux across the scale  $\Delta$  in the spectral space. As is shown in [52], in stationary turbulence with infinite Reynolds number, the ensemble average of Eq. (8) reduces to  $\langle \Pi_H \rangle = \epsilon_H$  when the filter scale falls in the inertial range. That is,  $\Pi_H$  controls the global balance of helicity in helical turbulence.

The behaviors of  $\Pi_H$  have been investigated in [11, 19]. The scaling properties of  $\Pi_H$  are documented. It is observed that the mean SGS helicity dissipation  $\langle \Pi_H \rangle$  is approximately constant in the inertial range, corresponding to a constant helicity flux across the spectrum (see also [52]). Also, it is found that reflectional symmetry in helical turbulence is asymptotically restored at small scales, due to helicity fluxes exchanging negative and positive helicity between the negative and positive helical wave components [11].

$\Pi_H$  is the tensor product of the two tensors  $\tau_{ij}$  and  $\tilde{R}_{ij}$ . Apart from the correlation between them, the relative orientation of the two tensors is another factor that controls the value of  $\Pi_H$ . The relative orientation of the two tensors can be characterized by the orientation of the eigen-frames associated with them. As  $\tau_{ij}$  and  $\tilde{R}_{ij}$  are both symmetric, they have each three real eigenvalues. The corresponding eigenvectors constitute two Cartesian coordinate frames. In what follows, we denote the eigenvalues of  $-\tau_{ij}$  by  $(-\tau)_\alpha$ ,  $(-\tau)_\beta$ , and  $(-\tau)_\gamma$ , and they are ordered so that  $(-\tau)_\alpha \geq (-\tau)_\beta \geq (-\tau)_\gamma$ . By definition  $\tau_{kk} = 0$ . The eigenvalues are thus related by  $(-\tau)_\alpha + (-\tau)_\beta + (-\tau)_\gamma = 0$ , and as a result  $(-\tau)_\alpha \geq 0$  and  $(-\tau)_\gamma \leq 0$ . The eigenvalues of  $\tilde{R}_{ij}$  are denoted similarly as  $R_\alpha \geq R_\beta \geq R_\gamma$ . Since vorticity is solenoidal, we also have  $R_\alpha + R_\beta + R_\gamma = 0$  and  $R_\alpha \geq 0 \geq R_\gamma$ . Corresponding to the eigenvalues, we use  $(-\boldsymbol{\tau})_\alpha$ ,  $(-\boldsymbol{\tau})_\beta$ , and  $(-\boldsymbol{\tau})_\gamma$  to denote the eigenvectors of  $-\tau_{ij}$ , and  $\mathbf{R}_\alpha$ ,  $\mathbf{R}_\beta$ , and  $\mathbf{R}_\gamma$  those of

$\tilde{R}_{ij}$ . The eigenvectors are normalized so that they have unit length. With these definitions, one can write the SGS helicity dissipation in terms of the eigenvalues and eigenvectors:

$$\begin{aligned} \Pi_H = & 2\{(-\tau)_\alpha R_\alpha [(-\tau)_\alpha \cdot \mathbf{R}_\alpha]^2 + (-\tau)_\alpha R_\beta [(-\tau)_\alpha \cdot \mathbf{R}_\beta]^2 + (-\tau)_\alpha R_\gamma [(-\tau)_\alpha \cdot \mathbf{R}_\gamma]^2 \\ & + (-\tau)_\beta R_\alpha [(-\tau)_\beta \cdot \mathbf{R}_\alpha]^2 + (-\tau)_\beta R_\beta [(-\tau)_\beta \cdot \mathbf{R}_\beta]^2 + (-\tau)_\beta R_\gamma [(-\tau)_\beta \cdot \mathbf{R}_\gamma]^2 \\ & + (-\tau)_\gamma R_\alpha [(-\tau)_\gamma \cdot \mathbf{R}_\alpha]^2 + (-\tau)_\gamma R_\beta [(-\tau)_\gamma \cdot \mathbf{R}_\beta]^2 + (-\tau)_\gamma R_\gamma [(-\tau)_\gamma \cdot \mathbf{R}_\gamma]^2\}. \end{aligned} \quad (10)$$

A similar expression for the SGS energy dissipation can be found in, e.g., [53]. In Eq. (10),  $(-\tau)_i \cdot \mathbf{R}_j \equiv \cos \theta_{ij}$ , where  $\theta_{ij}$  is the angle between the vectors  $(-\tau)_i$  and  $\mathbf{R}_j$  ( $i, j = \alpha, \beta, \gamma$ ). Eq. (10) thus shows that the SGS helicity dissipation depends on both the eigenvalues of the tensors  $\tilde{R}_{ij}$  and  $\tau_{ij}$ , and the relative orientation of the eigenvectors. Note, however, the nine inner products that appear in the above equation are not independent to each other. To fully characterize the relative orientation of the two eigen-frames, only three angles are needed, as will be introduced in next section.

One may attempt to understand the evolution of the eigenvalues and eigenvectors of  $\tilde{R}_{ij}$  from its dynamic equations. Tensor  $\tilde{R}_{ij}$  is the symmetric part of the vorticity gradient. Denoting the vorticity gradient  $\partial_j \tilde{\omega}_i$  by  $\tilde{G}_{ij}$ , the equation for  $\tilde{G}_{ij}$  can be found by taking the gradient of Eq. (7):

$$\begin{aligned} D_t \tilde{\mathbf{G}} = & \tilde{\mathbf{A}} \tilde{\mathbf{G}} - \tilde{\mathbf{G}} \tilde{\mathbf{A}} + \tilde{\boldsymbol{\omega}} \cdot \nabla \tilde{\mathbf{A}} + \nabla (\nabla \times \mathbf{T}) \\ & + \nu \nabla^2 \tilde{\mathbf{G}} + \nabla (\nabla \times \tilde{\mathbf{f}}), \end{aligned} \quad (11)$$

where  $\tilde{\mathbf{A}}$  is the filtered velocity gradient, with components  $\tilde{A}_{ij} = \partial_j \tilde{u}_i$ . The last three terms in Eq. (11) come from the effects of SGS motion, viscous diffusion, and external forces, respectively, while the first three represent the nonlinear self-stretching effects. The first and the third terms originate from the gradient of the vortex-stretching term  $\tilde{\mathbf{S}} \tilde{\boldsymbol{\omega}}$  in the vorticity equation (note that  $\tilde{\mathbf{S}} \tilde{\boldsymbol{\omega}} = \tilde{\mathbf{A}} \tilde{\boldsymbol{\omega}}$ ). The first term represents the contributions from the spatial variation in  $\tilde{\boldsymbol{\omega}}$ , while the third represents those from the spatial variation in  $\tilde{\mathbf{A}}$ . The second term, on the other hand, is due to the stretching of material lines accompanying that of the vortex lines, which tends to reduce the growth of vorticity gradients.

$\tilde{G}_{ij}$  can be decomposed into the sum of its symmetric part  $\tilde{R}_{ij}$  and the anti-symmetric tensor  $\tilde{\Xi}_{ij} \equiv (\tilde{G}_{ij} - \tilde{G}_{ji})/2$ . For the convenience of exposition, we will call  $\tilde{R}_{ij}$  the vorticity strain rate tensor. From  $\tilde{\Xi}_{ij}$ , one can define the dual vector  $\tilde{\boldsymbol{\xi}} = \nabla \times \tilde{\boldsymbol{\omega}}$  through  $\tilde{\Xi}_{ij} = -\epsilon_{ijk} \tilde{\xi}_k / 2$  [31]. It is well-known that  $\tilde{\boldsymbol{\xi}} = -\nabla^2 \mathbf{u}$  and as such is proportional to the viscous diffusion term in the NS equations. Thus these quantities, apart from characterizing the local topology of the vorticity field, also have dynamical significance. The equations for  $\tilde{R}_{ij}$

and  $\tilde{\xi}_i$  can be derived easily from the equation for  $\tilde{G}_{ij}$ . After some algebra, one finds

$$D_t \tilde{\mathbf{R}} = [\tilde{\mathbf{S}} \times \tilde{\boldsymbol{\xi}} - \tilde{\mathbf{R}} \times \tilde{\boldsymbol{\omega}}]^S + [\nabla(\nabla \times (\mathbf{T} + \tilde{\mathbf{f}}))]^S + \tilde{\boldsymbol{\omega}} \cdot \nabla \tilde{\mathbf{R}} + \nu \nabla^2 \tilde{\mathbf{R}}, \quad (12)$$

where superscript  $S$  denotes the symmetric part of the tensor.  $(\tilde{\mathbf{S}} \times \tilde{\boldsymbol{\xi}})_{ij} = \epsilon_{ikm} \tilde{S}_{kj} \tilde{\xi}_m$  and  $\tilde{\mathbf{R}} \times \tilde{\boldsymbol{\omega}}$  is similarly defined. For  $\tilde{\xi}_i$ , the equation reads:

$$D_t \tilde{\xi}_i = 2\epsilon_{ijk} \tilde{S}_{jl} \tilde{R}_{lk} + \frac{1}{2}(\tilde{\boldsymbol{\omega}} \times \tilde{\boldsymbol{\xi}})_i + \tilde{\boldsymbol{\omega}} \cdot \nabla \tilde{\omega}_i + \nu \nabla^2 \tilde{\xi}_i + \partial_{ij}^2 T_j - \nabla^2 (T_i + \tilde{f}_i). \quad (13)$$

Use has been made of the fact that  $\tilde{f}_i$  has to be divergence-free.

The eigenvalues of  $\tilde{G}_{ij}$  and  $\tilde{R}_{ij}$  are fully characterized by their tensorial invariants. Because vorticity is solenoidal, the traces of  $\tilde{R}_{ij}$  and  $\tilde{G}_{ij}$  are both zero. Thus they each have only two independent invariants. We define the following tensor invariants for  $\tilde{G}_{ij}$ :

$$\mathbf{I}_2^G \equiv -\text{Tr} \tilde{\mathbf{G}}^2 / 2, \quad \mathbf{I}_3^G \equiv -\text{Tr} \tilde{\mathbf{G}}^3 / 3, \quad (14)$$

and similarly for  $\tilde{R}_{ij}$ :

$$\mathbf{I}_2^R \equiv -\text{Tr} \tilde{\mathbf{R}}^2 / 2, \quad \mathbf{I}_3^R \equiv -\text{Tr} \tilde{\mathbf{R}}^3 / 3. \quad (15)$$

Note that these invariants correspond to the  $Q$  and  $R$  used in, e.g., [37]. The eigenvalues of  $\tilde{R}_{ij}$  are related to its invariants by

$$\mathbf{I}_2^R = -\frac{1}{2}(R_\alpha^2 + R_\beta^2 + R_\gamma^2), \quad \mathbf{I}_3^R = -R_\alpha R_\beta R_\gamma. \quad (16)$$

There are similar relations for  $\mathbf{I}_2^G$  and  $\mathbf{I}_3^G$ . But as the eigenvalues of  $\tilde{G}_{ij}$  may not be real numbers, we will not study the eigenvalues of  $\tilde{G}_{ij}$  directly.

The evolution of the eigenvalues of  $\tilde{G}_{ij}$  and  $\tilde{R}_{ij}$  can be inferred from the dynamics of the invariants, the so-called trace dynamics. The trace dynamics of the velocity gradient  $\tilde{A}_{ij}$  has been used extensively in the study of the local geometry of the velocity field (see e.g., [37, 40, 41, 54–57]). Its usefulness comes in part from the so-called restricted Euler (RE) model [37, 54, 58]. In the RE model, the Euler equation is truncated to retain only the nonlinear self-interaction of the velocity gradient and the isotropic part of the pressure Hessian tensor, so that the invariants of  $\tilde{A}_{ij}$  form a closed 2-dimensional dynamical system. The model is shown to reproduce a number of dynamical features of turbulence, and has been subjected to various studies and extensions. For  $\tilde{G}_{ij}$  and  $\tilde{R}_{ij}$ , it is tempting to also look into the trace dynamics, and the RE-type approximations. A truncation of the equation of  $\tilde{G}_{ij}$  [Eq. (11)] in the spirit of RE approximation retains only the first two terms on the

RHS. However, it is not difficult to find that, this truncated system leads to a trivial trace dynamics, in which the rates of changes of the invariants are zero. In other words, the straightforward generalization of the RE approximation to model  $\tilde{G}_{ij}$  does not yield useful results. Therefore, we will not continue to write down the equations for the invariants. In this paper we will focus on the analysis of the tensors and related quantities, and leave the analysis and modelling of the equations for future research.

A brief description of the simulations follows. We perform forced three dimensional pseudo-spectral DNS of isotropic turbulence in a  $[0, 2\pi]^3$  domain with periodic boundary conditions. Helicity and energy are injected into the flow field at constant rates, by the forcing term in the NS equations. The force is applied only to the low wavenumber modes  $|\mathbf{k}| \leq k_f \equiv 2$ . The details of the forcing term, in particular the method to inject helicity, are explained in our previous work [52]. The constant energy and helicity injection rates are  $\epsilon_f = 0.1$  and  $\epsilon_{H,f} = 0.3$ , respectively. Note that the helicity injection rate is limited by the inequality  $|\epsilon_{H,f}| \leq 2k_f\epsilon_f$  [10]. Thus the current value is close to the maximum. The statistics are calculated after the flow has achieved stationary state after a few eddy turn-over time-scales. For all simulations, the number of grid points is  $N^3 = 256^3$  with kinematic viscosity  $\nu = 0.0015$ . At stationary state the Taylor micro-scale Reynolds number is estimated as  $Re_\lambda \approx 190$ . The Kolmogorov length scale, denoted by  $\eta_K$ , is approximately 0.0136, so that  $\eta_K k_{\max} \approx 1.7$ . Thus the simulations are well-resolved [59]. The aliasing error is negligible for the statistics of the filtered data. Therefore we have not dealiased the simulations. The maximum resolved wavenumber is thus  $k_{\max} = N/2 = 128$ , and the grid size is  $\delta x = 2\pi/N = \pi/128$ . The time step size  $\delta t$  is adaptively chosen at each step to ensure  $\beta \equiv \delta t u_{\max}/\delta x \leq 0.15$ , where  $\beta$  is the Courant number and  $u_{\max}$  is the maximal velocity in the flow field at the given time step.

To compare the differences between helical and non-helical turbulence, simulations without helicity input are also conducted. The non-helical simulations are exactly the same as the helical ones apart from  $\epsilon_{H,f} = 0$ . Some of the results are also cross-checked with data obtained from simulations with negative helicity input, in which the helicity injection rate  $\epsilon_{H,f} = -0.3$ . In the analyses that follow, results for filter scales  $\Delta = 8\delta x$  and  $16\delta x$  will be documented, corresponding to  $\Delta x \approx 14.5\eta_K$  and  $30\eta_K$ , respectively. Throughout the analyses, the Gaussian filter is used [59].

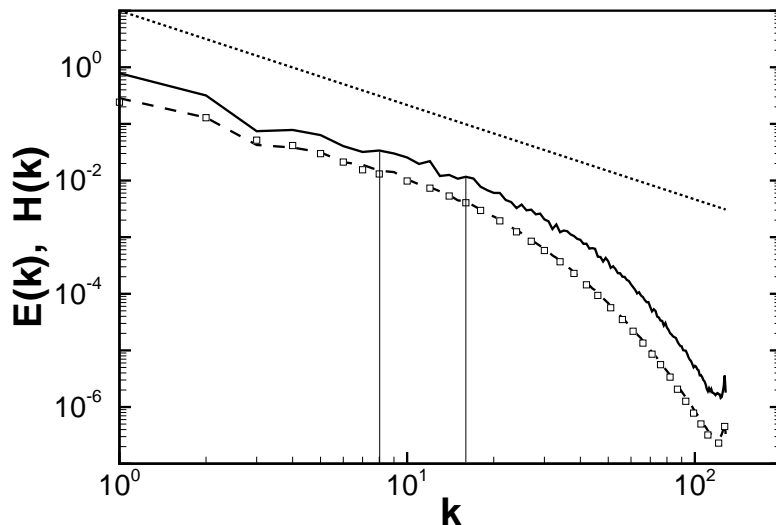


FIG. 1: Helicity and energy spectra. Solid line: helicity spectrum; dashed line: energy spectrum; symbols: energy spectrum in non-helical data; dotted line has a slope  $-5/3$ .

### III. ANALYSIS OF DNS DATA

#### A. Basic statistics

Some basic statistics are presented first. The energy and helicity spectra in the data sets are shown in Figure 1, which confirms the  $-5/3$  spectrum for helicity. The energy spectra in both helical and non-helical turbulence are plotted and they are nearly the same. The vertical lines mark the two filter scales  $8\delta x$  and  $16\delta x$  used in our analyses.

A so-called relative helicity can be used to characterize the degree of alignment between  $\mathbf{u}$  and  $\boldsymbol{\omega}$  (see, e.g. [12]). The relative helicity is defined as

$$h' \equiv h/(|\mathbf{u}||\boldsymbol{\omega}|) = \mathbf{u} \cdot \boldsymbol{\omega}/(|\mathbf{u}||\boldsymbol{\omega}|). \quad (17)$$

The PDF of  $h'$  in our current data set is shown in Figure 2. As comparison, the PDF is also calculated in a data set with the low wave number Fourier modes  $|\mathbf{k}| \leq k_f$  removed by high-pass filtering. The result is shown with dashed line in same figure. The results given in Figure 2 are consistent with previous research such as [12], i.e., the alignment between  $\mathbf{u}$  and  $\boldsymbol{\omega}$  comes predominantly from large-scale motions. The mean helicity is 0.69 in the filtered data, whereas it is 1.60 in the original DNS data. Thus the first two shells in the Fourier space contain more than 50% of the total helicity.

Figure 3 plots the mean SGS helicity and energy dissipations as functions of filter scale

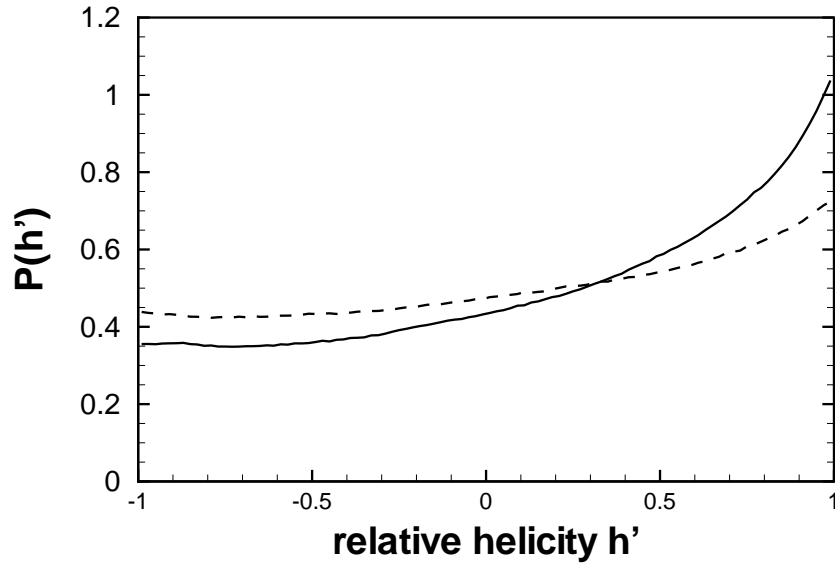


FIG. 2: Solid line: PDF of the relative helicity  $h'$ ; dashed line: PDF of  $h'$  obtained from the high-pass data with modes  $|\mathbf{k}| \leq k_f$  removed.

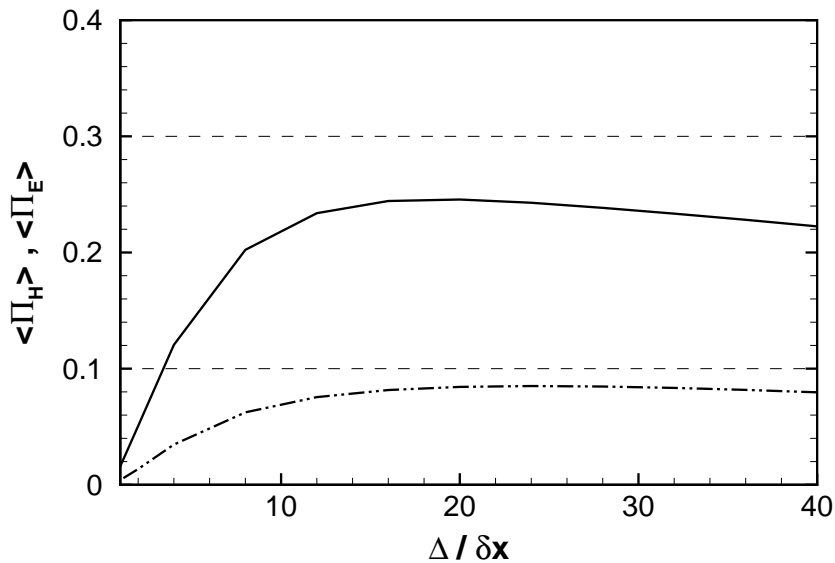


FIG. 3: Mean SGS helicity (solid line) and energy (dash-double-dotted line) dissipations at different filter scales.

$\Delta$ . The horizontal dashed lines denote the levels of helicity and energy injection rates. In the limit of infinite Reynolds number, the mean SGS dissipations should equal the injection rates when  $\Delta$  falls in the inertial range. In our results we observe plateaus for the two curves that are somewhat lower than the injection values. The discrepancy is likely due to viscous

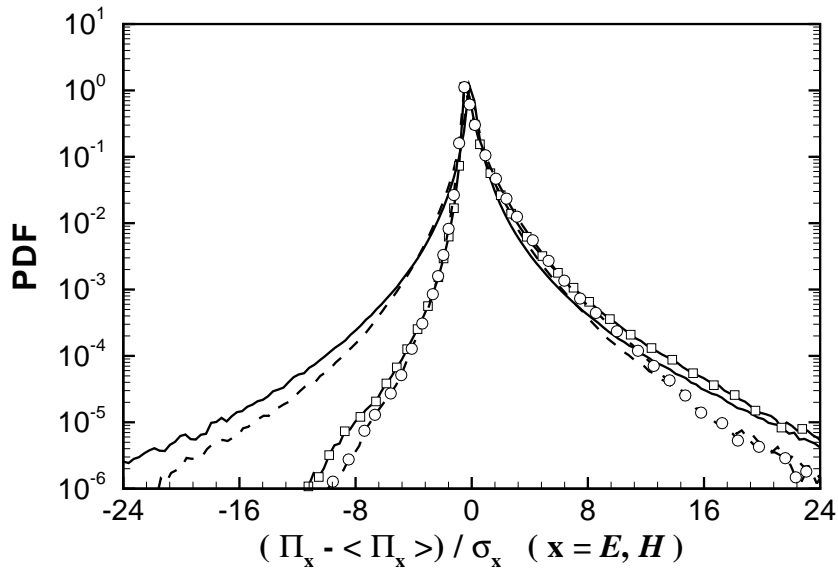


FIG. 4: PDFs of normalized SGS helicity (lines) and energy (symbols) dissipations.  $\Delta = 8\delta x$ : solid line and squares;  $\Delta = 16\delta x$ : dashed line and circles.  $\sigma_E$  and  $\sigma_H$  stand for the root-mean-square values of  $\Pi_E$  and  $\Pi_H$ , respectively.

effects. The PDFs of the normalized SGS dissipations, at  $\Delta = 8\delta x$  and  $16\delta x$ , are plotted in Figure 4. One can observe that the distributions are all skewed towards the positive axis direction. The PDFs for the SGS helicity dissipation have wider tails than those for the SGS energy dissipation, especially for the left tails. These features are consistent with the observations made in [19], where the intermittency of helicity cascade is investigated in detail.

### B. Tensor invariants of the vorticity gradient

Although the vorticity gradient  $\tilde{G}_{ij}$  does not appear explicitly in the expression of SGS helicity dissipation, it contains the complete information needed to infer the local structures of the vorticity field, whereas  $\tilde{R}_{ij}$  characterizes only the straining of the vortex lines. Thus we present first the results of the invariants of  $\tilde{G}_{ij}$ ,  $\mathbf{I}_2^G$  and  $\mathbf{I}_3^G$ . To begin with, we briefly explain the relation between the local structures of the vorticity field and the values of  $\mathbf{I}_2^G$  and  $\mathbf{I}_3^G$ . Given the values of  $\mathbf{I}_3^G$  and  $\mathbf{I}_2^G$  at a given spatial location, say  $\mathbf{x}^0$ , one can deduce the local topology of the vortex lines around  $\mathbf{x}^0$ , in the same way as one infers the local streamline patterns from the values of the invariants of the velocity gradient  $\tilde{\mathbf{A}}$ . The local streamline patterns in different regions in the phase plane of the invariants of  $\tilde{\mathbf{A}}$  have been revealingly illustrated in, e.g., [37, 41]. The diagram, adapted to our problem, is shown in Figure 5.

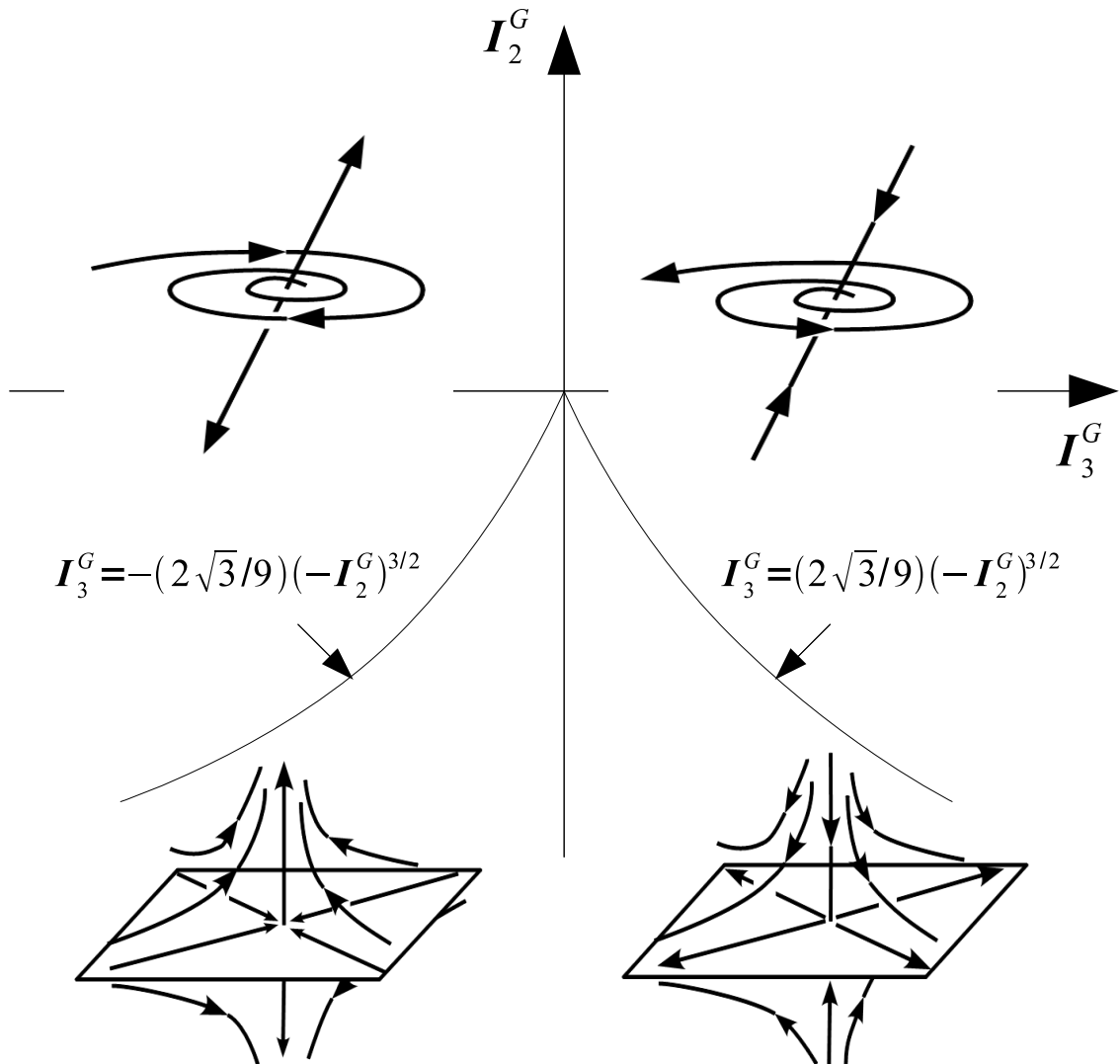


FIG. 5: The local topology of the vortex lines in different regions of the phase plane  $(\mathbf{I}_3^G, \mathbf{I}_2^G)$  based on ‘relative vorticity’ (see text).

The two curves in the third and fourth quadrants are the so-called Vieillefosse tails, defined as  $\mathbf{I}_3^G = \pm(2\sqrt{3}/9)(-\mathbf{I}_2^G)^{3/2}$ . The Vieillefosse tails, together with the  $\mathbf{I}_2^G$  axis, divide the phase plane into four parts with distinct local vortex line patterns, as illustrated in Figure 5. Around point  $\mathbf{x}^0$ , locally the vorticity field can be approximated by linear approximation  $\tilde{\omega}_i(\mathbf{x}) \approx \tilde{\omega}_i(\mathbf{x}^0) + \tilde{G}_{ij}(\mathbf{x}^0)(x_j - x_j^0)$ . Sketched in Figure 5 are vortex lines calculated from the ‘relative’ vorticity  $\tilde{\omega}_i^*$  defined as

$$\tilde{\omega}_i^*(\mathbf{x}) \equiv \tilde{\omega}_i(\mathbf{x}) - \tilde{\omega}_i(\mathbf{x}^0) \approx \tilde{G}_{ij}(\mathbf{x}^0)(x_j - x_j^0), \quad (18)$$

which is specified by  $\tilde{G}_{ij}(\mathbf{x}^0)$ . Under linear approximation, the actual vortex line patterns (i.e., those calculated from  $\tilde{\omega}_i$ ) are the same as the ones shown in Figure 5, except being translated uniformly by a displacement proportional to the local vorticity  $\tilde{\omega}_i(\mathbf{x}^0)$ .

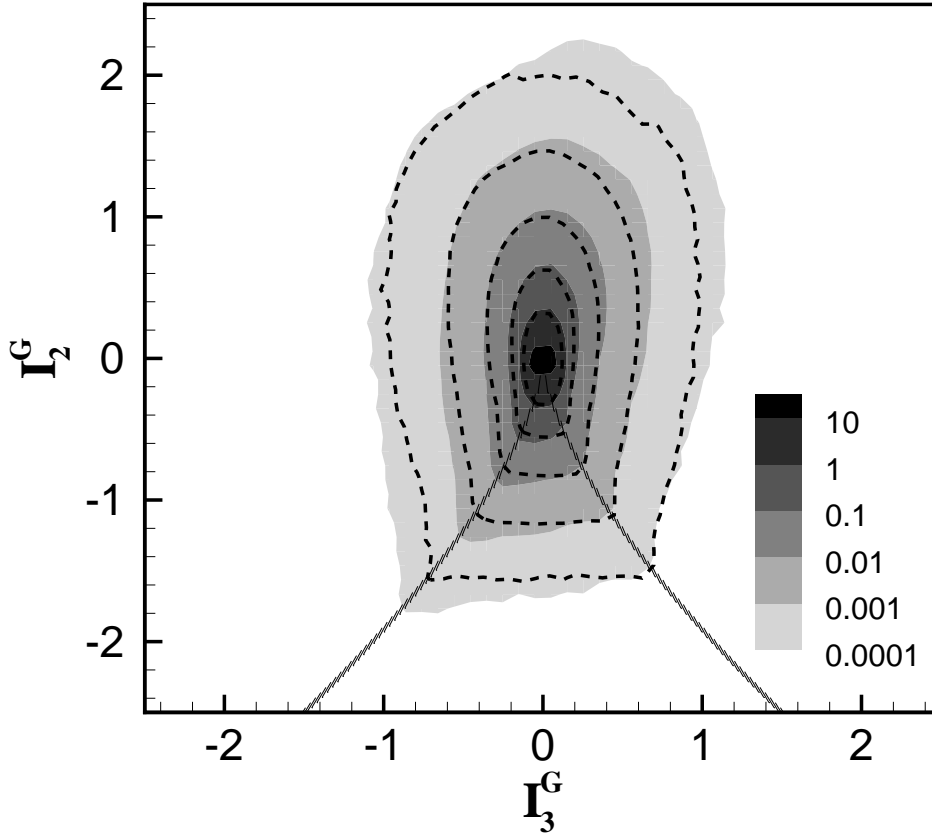


FIG. 6: The joint PDF of the invariants  $\mathbf{I}_3^G$  and  $\mathbf{I}_2^G$ . Contours in grey-scales: helical turbulence; dashed lines: non-helical,  $\Delta = 16\delta x$ . The two solid lines correspond to the Vieillefosse tails.

Figure 6 plots the joint PDF of  $\mathbf{I}_2^G$  and  $\mathbf{I}_3^G$ , for  $\Delta = 16\delta x$ . The invariants are normalized by  $\sigma_G^2$  and  $\sigma_G^3$ , respectively, where  $\sigma_G \equiv \langle \tilde{G}_{ij}\tilde{G}_{ij} \rangle^{1/2}$ . The two Vieillefosse tails are also drawn with solid lines. The PDF for helical turbulence is shown in grey scales, and that for non-helical turbulence is shown with dashed lines. For the PDF in non-helical turbulence, the shapes of the contours are similar to those of a Gaussian field (not shown), although for the former there is a much higher peak at the origin. The PDF is symmetric with respect to the  $\mathbf{I}_2^G$ -axis. The symmetry of the non-helical result is a consequence of the reflectional symmetry of the flow field. As  $\mathbf{I}_3^G$  is a pseudo-scalar, it takes the opposite sign in the reflection of the flow field. In other words, wherever it is positive (negative) in the original flow field, it is negative (positive) in the image flow field. As a consequence, the joint PDF is mapped onto

its mirror image with respect to the  $\mathbf{I}_2^G$  axis. However, in non-helical turbulence, the joint PDF should not change under a reflection transformation. Thus the joint PDF has to be symmetric with respect to the  $\mathbf{I}_2^G$  axis. On the other hand, the PDF in helical turbulence is not bounded by the constraint of reflectional invariance. Figure 6 shows indeed that the joint PDF develops a skewed distribution. The probabilities for the events in the first and the third quadrants are increased compared with non-helical data. In the third quadrant, the biggest difference is observed around the Vieillefosse tail. Referring to Figure 5, we find that, in helical turbulence, it is more probable to observe two types of local vortex structures. The first one corresponds to the structures around the left Vieillefosse tail, where the vortex lines converge from two directions and are extended along the third direction. The second one corresponds to the structures on the upper-right part of the phase plane, where the vortex lines form spirals around a direction along which the vorticity decreases.

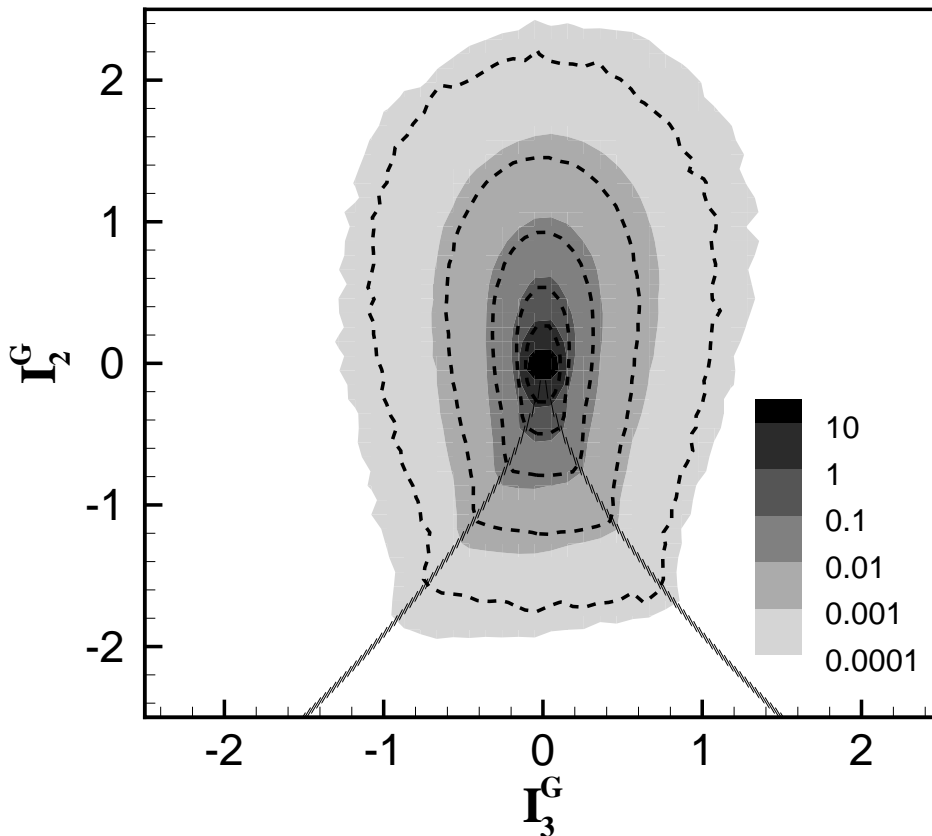


FIG. 7: Same as Figure 6, but for  $\Delta = 8\delta x$ .

Figure 7 shows the same results as in Figure 6 but for filter scale  $\Delta = 8\delta x$ . At smaller scales, we observe that the distribution of the invariants in helical turbulence becomes more

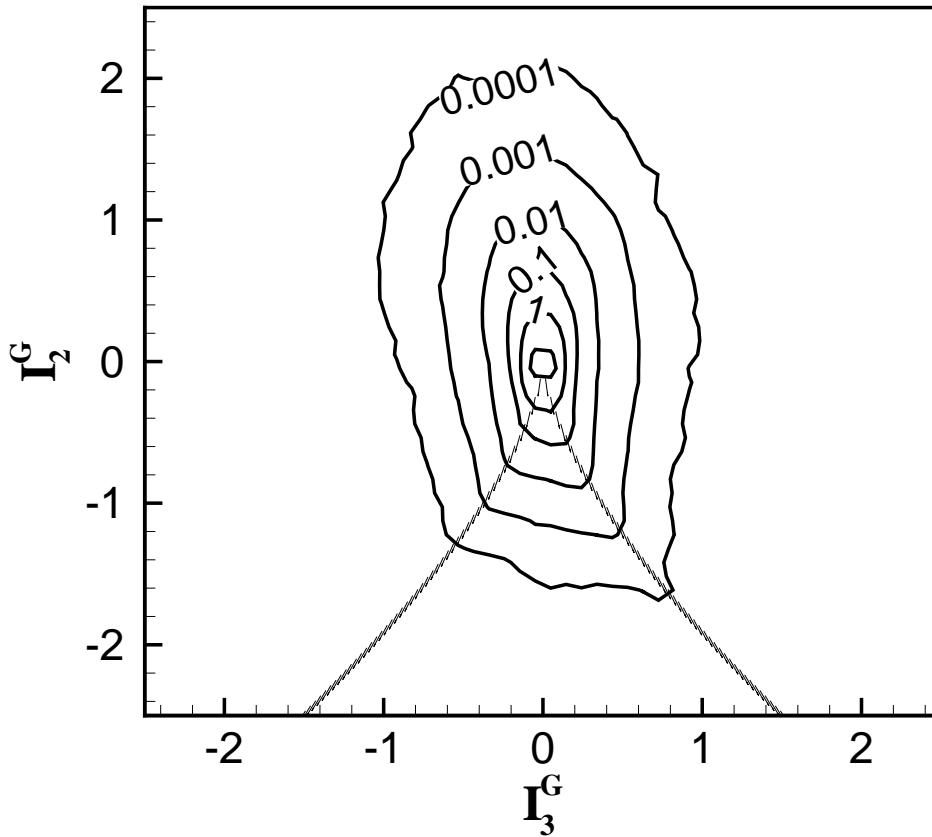


FIG. 8: Same as Figure 6, but for data with negative helicity injection rate  $\epsilon_{H,f} = -0.3$ .

intermittent than in non-helical turbulence. For helical turbulence, it is again more probable to observe vortex structures near the left Vieillefosse tail and the upper-right quadrant, even though the asymmetry in the distribution appears to slightly decrease.

We note that the probabilities of observing different local vortical structures depend on the sign of the helicity injection rate. To illustrate this point, we conduct simulations with negative helicity injection rate  $\epsilon_{H,f} = -0.3$ , as mentioned previously. The joint PDF of  $I_3^G$  and  $I_2^G$  calculated from this dataset is presented in Figure 8 for  $\Delta = 16\delta x$ . With the sign of helicity reversed, the distribution skews towards the opposite direction, compared with Figure 6. It becomes more probable to observe local vortex structures with vortex lines expanding in two directions and contracting along the third direction, and those with vortex lines winding around a direction along which the vorticity increases (c.f. Figure 5).

We now return to the analysis of helical data with positive helicity input. The above results focus on the difference in local vortical structures between helical and non-helical turbulence. The next question is how the difference correlates with helicity cascade. To

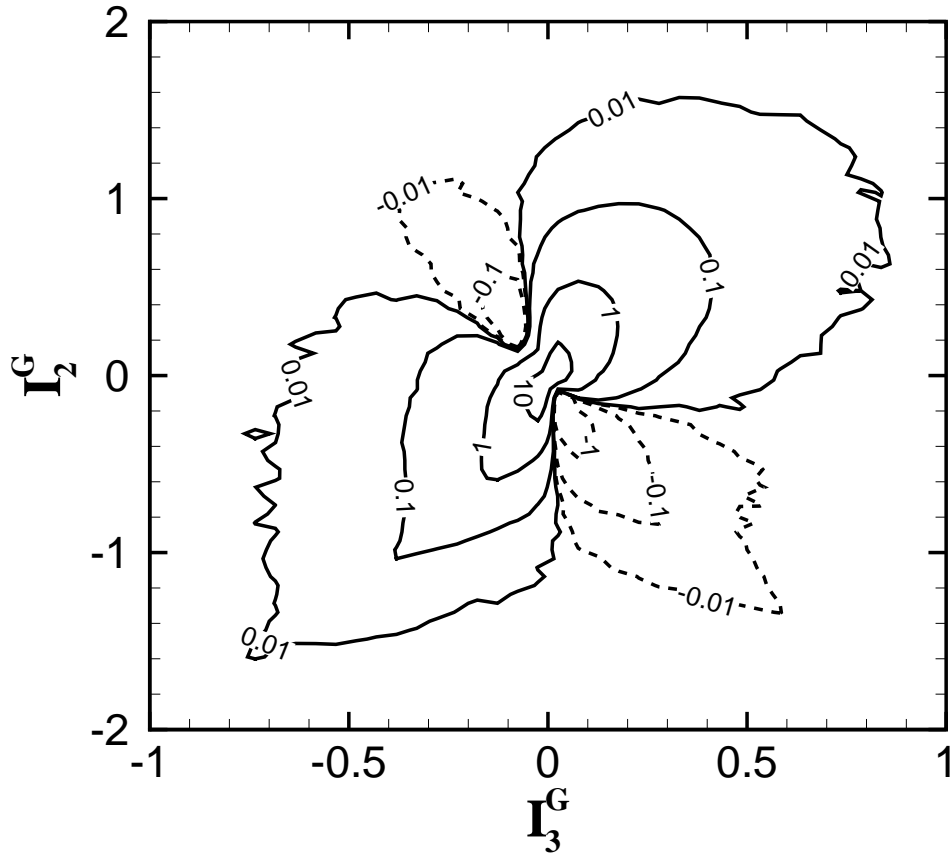


FIG. 9: The averaged SGS helicity dissipation rate conditioned on values of  $\mathbf{I}_3^G$  and  $\mathbf{I}_2^G$ , normalized by the mean SGS helicity dissipation and weighted with the joint PDF of  $\mathbf{I}_3^G$  and  $\mathbf{I}_2^G$ :  $P(\mathbf{I}_3^G, \mathbf{I}_2^G) \langle \Pi_H | \mathbf{I}_3^G, \mathbf{I}_2^G \rangle / \langle \Pi_H \rangle$ .  $\Delta = 16\delta x$ . Positive contours are shown with solid lines, negative with dashed lines.

shed light on this question, we examine the SGS helicity dissipation rate conditioned on the values of  $\mathbf{I}_3^G$  and  $\mathbf{I}_2^G$ . Figure 9 and 10 show the results for helical and non-helical turbulence at  $\Delta = 16\delta x$ , respectively. Results at  $\Delta = 8\delta x$  (not shown) are similar. For non-helical turbulence, we observe that the conditional dissipation is positive in both the first and the third quadrants, and is negative in the second and the fourth ones. In particular, the conditional dissipation tends to be positive around the left Vieillefosse tail, and negative around the right one. The distribution is approximately anti-symmetric with respect to both coordinate axes. In helical turbulence, the symmetry in the distribution is broken. The dissipation in the first and third quadrants is much stronger, while the magnitudes of the negative values in the second and fourth quadrants are significantly reduced. The comparison indicates that local vortical structures in the first and third quadrants are responsible for

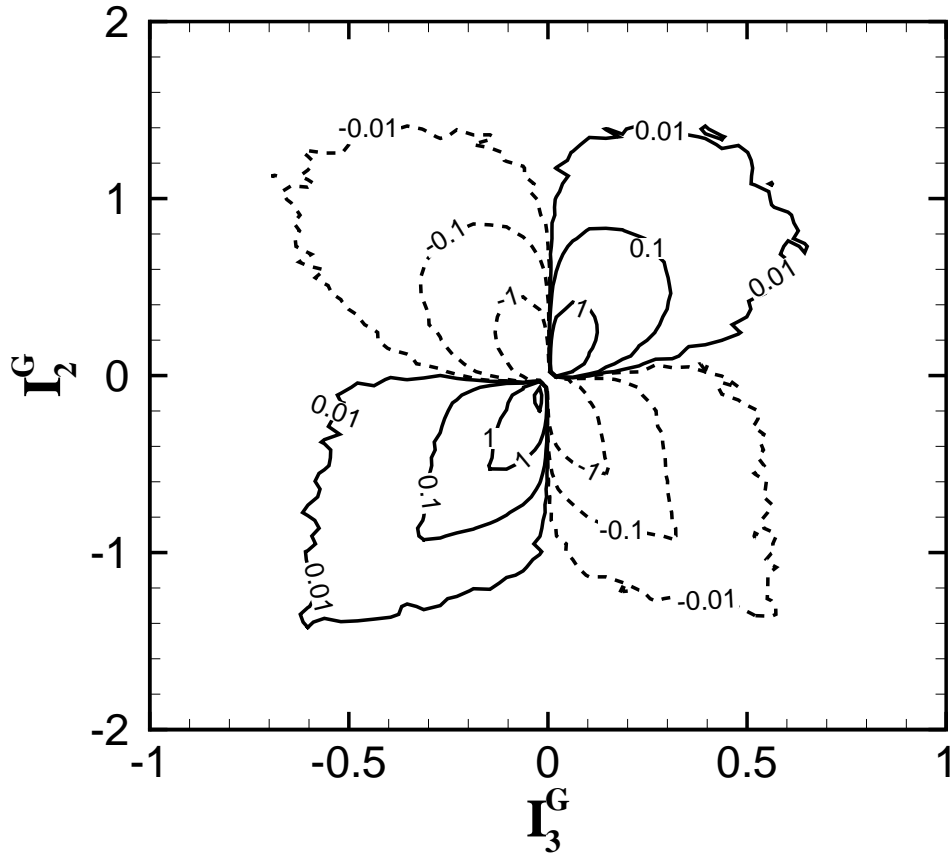


FIG. 10: Same as Figure 9 but for non-helical data. The distribution is normalized by the same  $\langle \Pi_H \rangle$  used in Figure 9.

generating positive SGS helicity dissipation, while those in the second and fourth are for negative one. This correspondence holds in both helical and non-helical turbulence. In helical turbulence, the positive fluctuations in SGS helicity dissipation become stronger. Together with Figure 6, we see that in helical turbulence it is more probable to observe stronger positive fluctuations in the SGS helicity dissipation, compared with non-helical turbulence. This difference is consistent with the need to generate a positive mean dissipation.

Figure 11 and 12 show the joint PDFs of  $\mathbf{I}_3^G$  and  $\mathbf{I}_2^G$  in helical turbulence conditioned on positive and negative SGS helicity dissipations, respectively. When conditioned on positive SGS helicity dissipation, i.e.,  $\Pi_H > 0$ , the asymmetry observed in the unconditional PDF (Figure 6) is further increased. That is, the events around the left Vieillefosse tail and in the upper-right quadrant now happen more frequently. When conditioned on  $\Pi_H < 0$ , asymmetry of the PDF switches towards the other direction. It becomes more probable to observe events around the right Vieillefosse tail and in the upper-left part of the phase

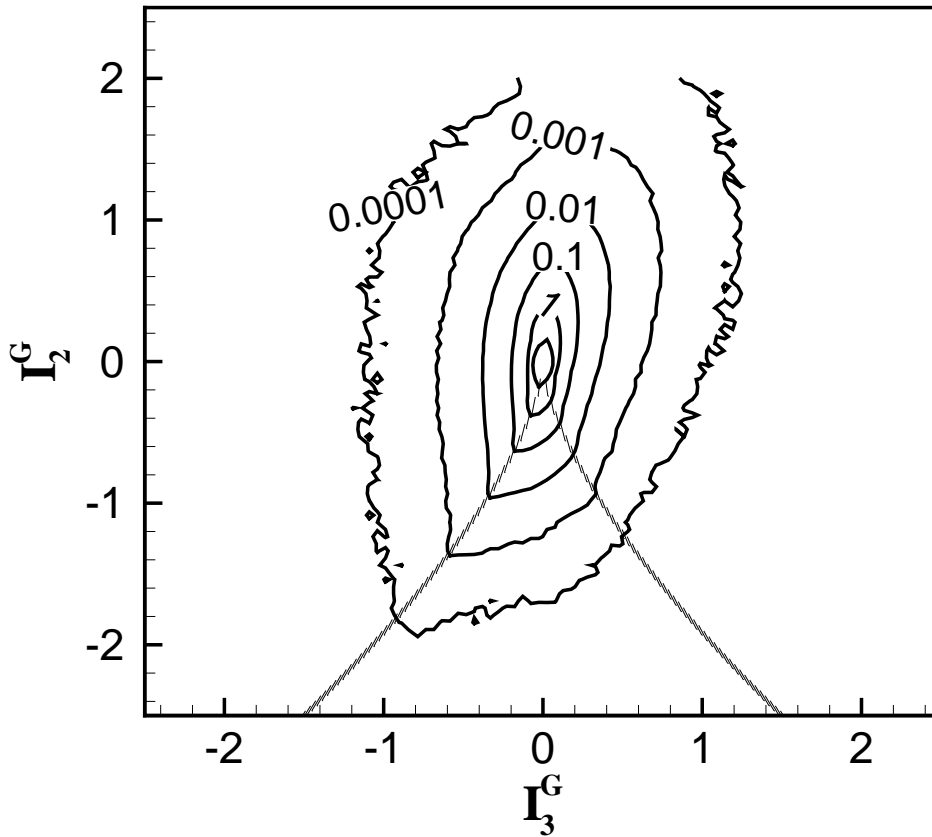


FIG. 11: The joint PDF of  $I_3^G$  and  $I_2^G$  conditioned on positive SGS helicity dissipation rate for the helical data.  $\Delta = 16\delta x$ .

plane. These results further confirm the correlation between the local vortex structures and the values of the SGS helicity dissipation observed in Figures 9 and 10. For non-helical turbulence, the conditional PDFs (not shown here) also display skewed distributions, even though the unconditional PDF is symmetric. The PDF conditioned on  $\Pi_H > 0$  also shows higher probabilities in the first and the third quadrants. However, compared with helical turbulence, the asymmetry is weaker. On the other hand, the PDF conditioned on  $\Pi_H < 0$  also shows a skewed distribution, with higher probabilities for the events in the second and the fourth quadrants. Compared with the conditional PDF for helical turbulence shown in Figure 12, the skewness is stronger. The average of the two conditional PDFs is the same as the unconditional PDF shown by the dashed lines in Figure 6, which is expected, since in non-helical turbulence the probabilities to observe positive and negative SGS helicity dissipation are equal.

The picture emerging from the above analyses is that the local structures of the vorticity

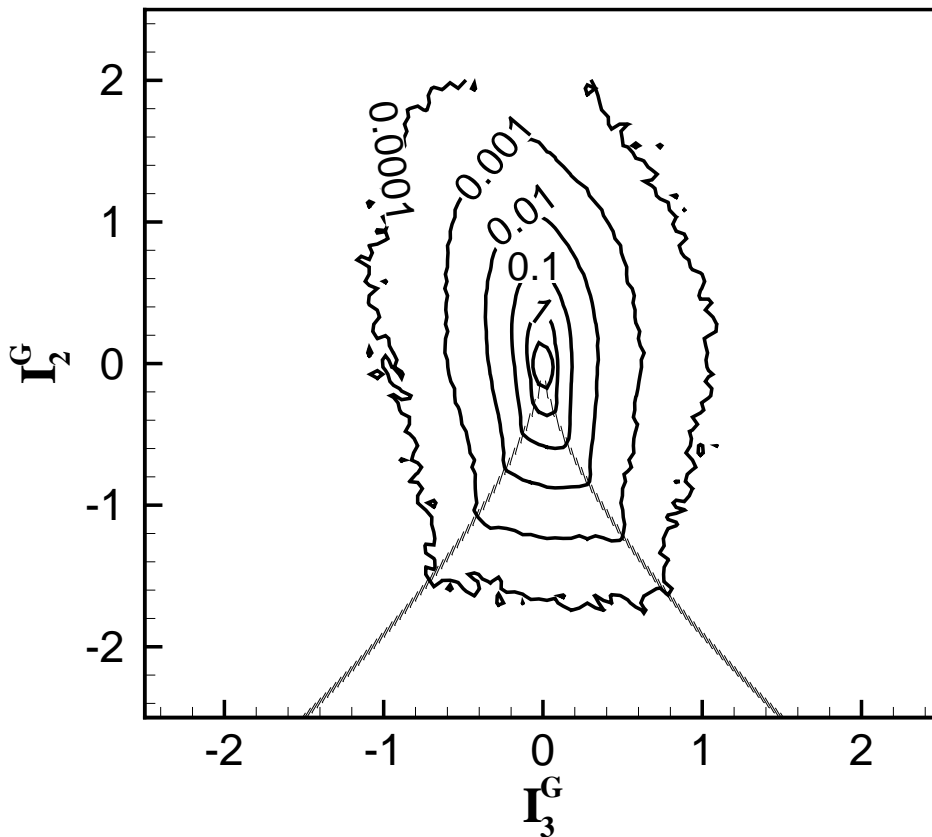


FIG. 12: Same as Figure 11 but conditioned on negative SGS helicity dissipation.

field and the SGS helicity dissipation fluctuations are correlated. The correlation is observed in both helical and non-helical turbulence. In helical turbulence with positive helicity input, it is more probable to observe positive SGS helicity dissipation (see Fig. 4). Due to the correlation, it is thus also more probable to observe certain vortical structures (those in the first and the third quadrants of the  $(\mathbf{I}_2^G, \mathbf{I}_3^G)$  plane). This in turn leads to asymmetry in a number of statistics. In other words, the asymmetry in helical turbulence originates from the imbalance of positive and negative SGS helicity dissipation.

It appears not yet possible to obtain a dynamical explanation for the correlation starting from first principles. Here, we provide a qualitative explanation for a certain part of the correlation, based on a simple dynamical model. We focus on the events around the Vieillefosse tails. As one has seen in both Figure 9 and 10, the SGS helicity dissipation tends to be positive around the left Vieillefosse tail and be negative around the right one. On the left tail, and the region between it and the  $\mathbf{I}_2^G$ -axis, the gradient of vorticity  $\tilde{G}_{ij}$  has one positive and two negative eigenvalues. Therefore, around a point in this region, the vortex lines

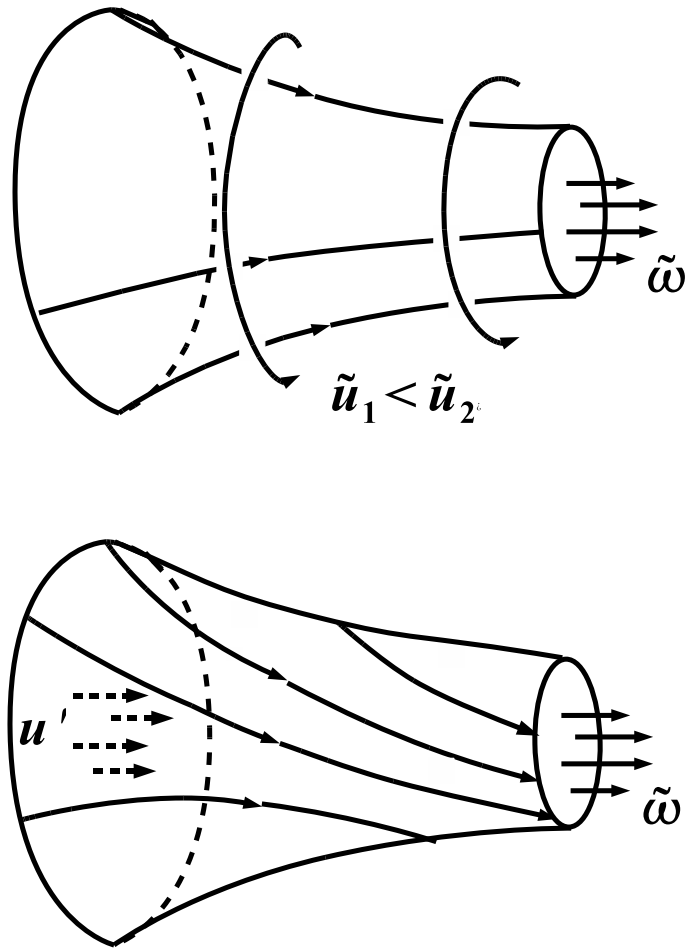


FIG. 13: Illustration of a converging vortex tube and its induced velocity (top). The vortex tube will be twisted by its induced velocity, and hence generates SGS helicity dissipation (bottom).

form a converging vortex tube, as illustrated in the top part of Figure 13. The magnitude of vorticity, then, has to increase along the tube. As a consequence, the induced velocity around the tube also increases along the tube, which thus stretches and twists the vortex lines so that they form a right-handed screw around the tube, as sketched in the bottom part of Figure 13. The vorticity on the twisted vortex lines has a component along the circumferential direction of the vortex tube, which then induces velocity fluctuations along the direction of the vortex tube. As the direction of the induced velocity is the same as the vorticity, it means that positive helicity fluctuations at smaller scales, and hence positive SGS helicity dissipation, have been generated. Therefore, converging vortex tubes tend to produce positive SGS helicity dissipation through their self-induced motions, which in turn

generates the correlation we observe around the left Vieillefosse tail.

Note that, the observation that twisted vortex tubes can generate small-scale helicity fluctuations has been made in [31]. Here, by looking into the eigenvalues of the vorticity gradient, we further elucidate how the twisted vortex tubes emerge from their self-induced motions. The correlation between negative SGS helicity dissipation and the right Vieillefosse tail can be explained in the same way.

### C. Invariants and eigenvalues of the vorticity strain rate tensor

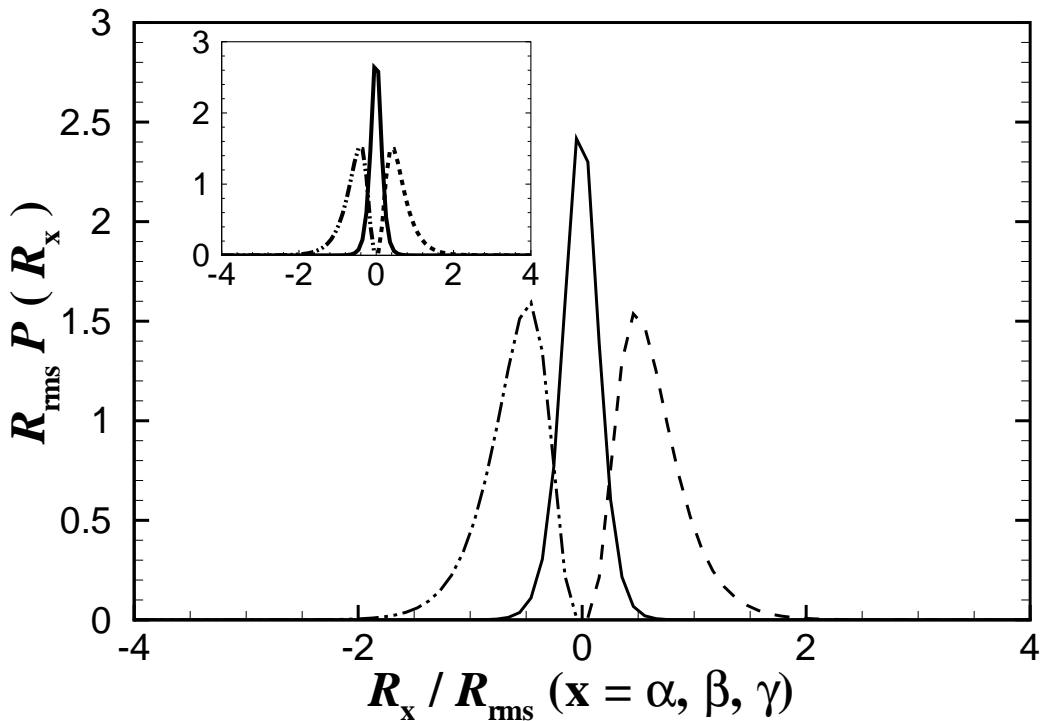


FIG. 14: PDF of the eigenvalues of  $\tilde{R}_{ij}$  at filter scale  $\Delta = 16\delta x$  and  $\Delta = 8\delta x$  (inset), normalized by  $R_{\text{rms}}$  defined in text. Solid line:  $R_\beta$ ; dashed:  $R_\alpha$ ; dash-double-dotted:  $R_\gamma$ .

The analysis of the vorticity gradient  $\tilde{G}_{ij}$  is now extended to consider  $\tilde{R}_{ij}$ , the vorticity strain rate tensor. As  $\tilde{R}_{ij}$  is a symmetric tensor, its eigenvalues are real numbers. Figure 14 plots the PDFs of the normalized eigenvalues, calculated at filtered scale  $\Delta = 16\delta x$ . The normalization factor  $R_{\text{rms}}$  for the three eigenvalues is defined as:

$$R_{\text{rms}} \equiv \langle \tilde{R}_{ij} \tilde{R}_{ij} \rangle^{1/2} = \langle (R_\alpha^2 + R_\beta^2 + R_\gamma^2) \rangle^{1/2}. \quad (19)$$

The inset shows the corresponding results at  $\Delta = 8\delta x$ . By definition  $R_\alpha \geq 0$  and  $R_\gamma \leq 0$ .

$\Delta/\delta x$	16	8	0
Case 1:	-0.26	-0.30	-0.25
Case 2:	0.017	0.019	0.013
Case 3:	-0.18	-0.26	-0.27

TABLE I: The mean  $R_\beta$  at different scales for different data sets. Case 1: Helical data; Case 2: Non-helical data; Case 3: High-pass filtered helical data with modes  $|\mathbf{k}| \leq k_f = 2$  removed.

On the other hand,  $R_\beta$  can take both positive and negative values. The results for  $\Delta = 8\delta x$  is similar to those for  $\Delta = 16\delta x$ , with slightly more spiky distributions.

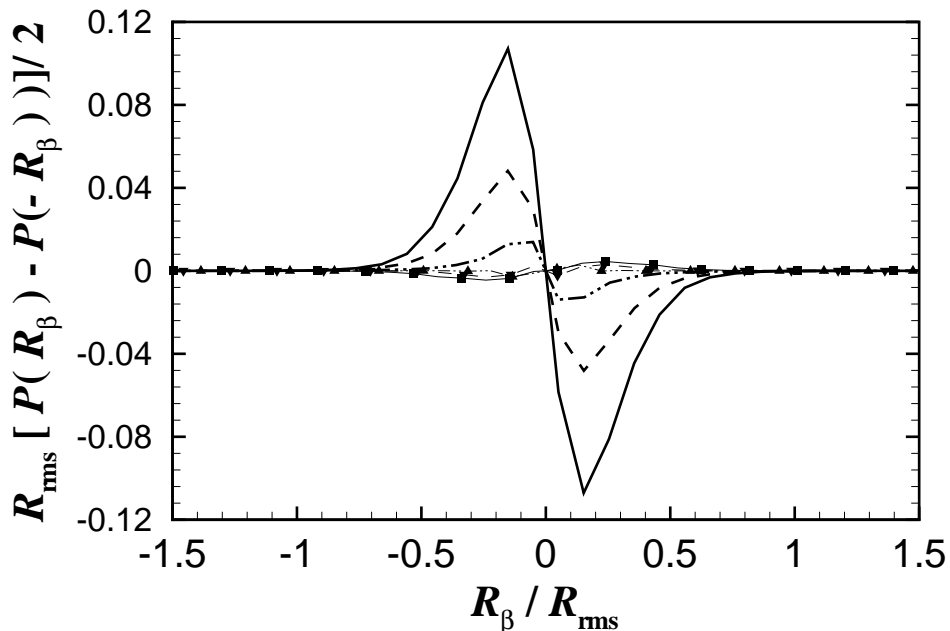


FIG. 15: Antisymmetric part of the PDF of  $R_\beta$  defined as  $R_{\text{rms}}[P(R_\beta) - P(-R_\beta)]/2$ . Lines: helical turbulence; symbols: non-helical turbulence. Solid line and deltas:  $\Delta = 16\delta x$ , dashed line and gradients:  $\Delta = 8\delta x$ ; dash-double-dotted line and squares : unfiltered data.

Note that  $\tilde{R}_{ij}$  is a pseudo-tensor. Thus, in turbulence with reflectional symmetry, the distribution of  $R_\beta$  should be symmetric, whereas in helical turbulence  $R_\beta$  is allowed to develop asymmetric distribution. Therefore, it is interesting to check if there is indeed asymmetry in the distribution of  $R_\beta$ . Figure 15 plots the anti-symmetric part of the PDFs of the normalized  $R_\beta$ , i.e.  $R_{\text{rms}}[P(R_\beta) - P(-R_\beta)]/2$ , at several filter scales. The distributions in both helical and non-helical turbulence are compared. The figure indeed shows that the PDFs of  $R_\beta$  are not symmetric. Instead,  $R_\beta$  is more probable to take negative values. On

the other hand, the results in non-helical turbulence, shown by symbols, are essentially zero, implying no deviation from reflectional symmetry.

The mean value of  $R_\beta$ , denoted as  $\langle R_\beta \rangle$  are given in Table I. Consistent with Figure 15,  $\langle R_\beta \rangle$  are negative in helical turbulence (Case 1), and are an order of magnitude bigger than the values in non-helical turbulence (Case 2). Interestingly, the values are nearly the same at three different scales, implying that the effects of helicity are felt down to the smallest scales. The last row shows  $\langle R_\beta \rangle$  calculated from a high-pass filtered data set, where the Fourier modes  $|\mathbf{k}| \leq k_f$  are removed (c.f. Figure 2). As has been shown in Figure 2, a large portion of helicity is contained in the forcing scales, and the alignment between  $\mathbf{u}$  and  $\boldsymbol{\omega}$  is significantly reduced when the forcing scales are removed. On the other hand, the same filtering leaves  $\langle R_\beta \rangle$  nearly unchanged. Thus, we conclude that the skewed PDFs of  $R_\beta$  come from small-scale motions in helical turbulence.

In regions where the vortex lines are dominantly strained, the eigenvalues of  $\tilde{R}_{ij}$  can be approximately related to the shapes of the vortex lines. That  $\tilde{R}_{ij}$  has two negative eigenvalues implies that the vortex lines tend to converge from two directions. The results in Figure 15 and Table I thus show that in these regions the vortex lines are more probable to form converging vortex tubes (see Figure 13). This is consistent with results obtained from the vorticity gradient  $\tilde{G}_{ij}$ .

Figure 16 plots the joint PDF of  $\mathbf{I}_2^R$  and  $\mathbf{I}_3^R$  for both helical and non-helical turbulence, shown in grey scales and dashed lines, respectively. The two invariants are related by inequality  $3\sqrt{6}|\mathbf{I}_3^R| \leq (-2\mathbf{I}_2^R)^{3/2}$  [60, 61], therefore the distribution is non-zero only in the wedge bounded by the Vieillefosse tails. Similar to the joint PDF of  $\mathbf{I}_3^G$  and  $\mathbf{I}_2^G$ , Figure 16 shows that the joint PDF of  $\mathbf{I}_3^R$  and  $\mathbf{I}_2^R$  is also asymmetric in helical turbulence. Higher probabilities are observed for events near the left Vieillefosse tail. It is more probable to observe negative  $\mathbf{I}_3^R$ , implying that  $R_\beta$  is more likely to be negative, consistent with our previous results in terms of the PDFs of  $R_\beta$ . For non-helical turbulence the distribution is symmetric.

The SGS helicity dissipation conditioned on  $\mathbf{I}_3^R$  and  $\mathbf{I}_2^R$  is shown in Figure 17 for helical turbulence, and in Figure 18 for non-helical turbulence. In both cases, positive values are observed mostly in the left half of the plane with  $\mathbf{I}_3^R < 0$ , while negative values are observed in the right half. Thus, there exists negative correlation between the SGS helicity dissipation and  $\mathbf{I}_3^R$  (and hence  $R_\beta$ ). The result for non-helical turbulence is anti-symmetric with respect to the  $\mathbf{I}_2^R$ -axis. In helical turbulence positive dissipation is observed in a larger domain and with higher magnitudes.

The geometry of the tensor  $\tilde{R}_{ij}$  can be studied with a nondimensional parameter  $R^*$ ,

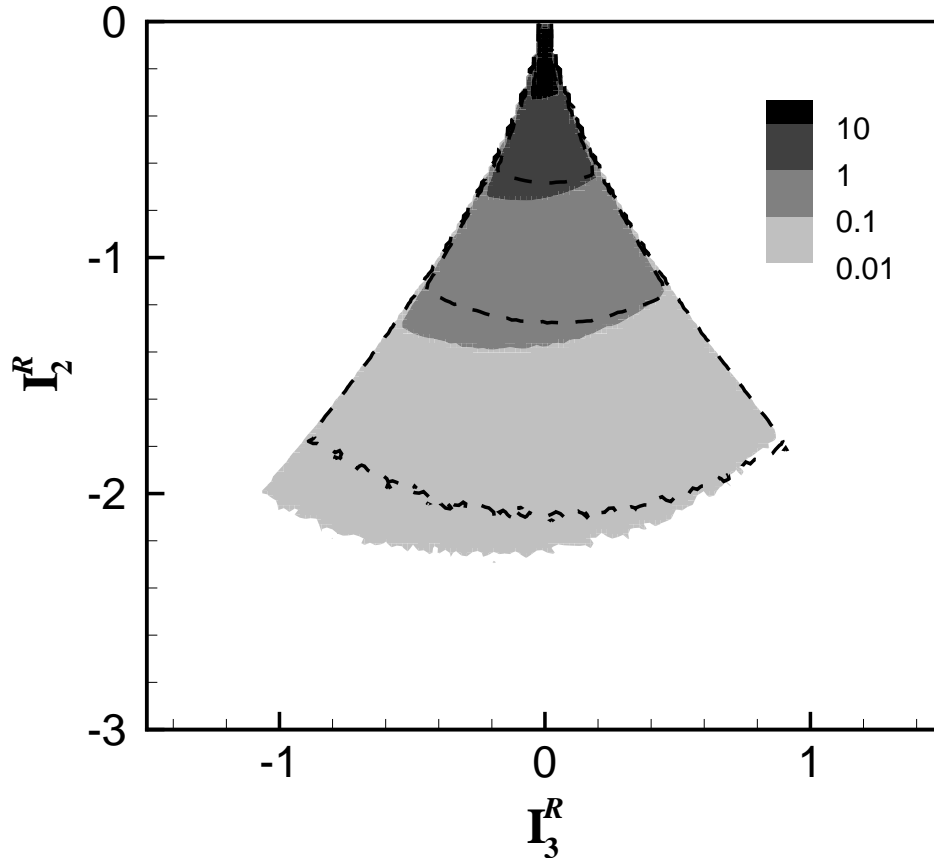


FIG. 16: The joint PDF of the invariants of  $\tilde{R}_{ij}$ ,  $\mathbf{I}_2^R$  and  $\mathbf{I}_3^R$ .  $\Delta = 16\delta x$ . Grey-scales: helical turbulence; dashed lines: non-helical turbulence.

defined as [61]

$$R^* = \frac{-3\sqrt{6}R_\alpha R_\beta R_\gamma}{(R_\alpha^2 + R_\beta^2 + R_\gamma^2)^{3/2}} = \frac{3\sqrt{6}\mathbf{I}_3^R}{(-2\mathbf{I}_2^R)^{3/2}}. \quad (20)$$

Similar parameters have already been used to investigate the geometry of the strain rate tensor and the SGS stress tensor [33, 61].  $R^*$  is bounded between  $-1$  and  $1$ , i.e.,  $R^* \in [-1, 1]$ . When  $R^* = 1$ , the ratio between the eigenvalues is  $R_\alpha : R_\beta : R_\gamma = 1 : 1 : -2$ , corresponding to axisymmetric expansion of the vortex lines, and also to the right Vieillefosse tail in the  $(\mathbf{I}_3^R, \mathbf{I}_2^R)$  plane. On the other hand,  $R^* = -1$  corresponds to axisymmetric contraction and the left Vieillefosse tail. In a Gaussian field, the PDF of  $R^*$  is uniform. Thus deviation from a uniform distribution comes from the dynamics of turbulence.

Figure 19 plots the joint PDF of  $R^*$  and  $\Pi_H$ , the SGS helicity dissipation. The result from helical turbulence is shown with grey scales while non-helical result is plotted with dashed lines. The first observation is that the distribution of  $\Pi_H$  shifts towards the negative direction when  $R^*$  is increases, in both datasets. That is, there exists negative correlation

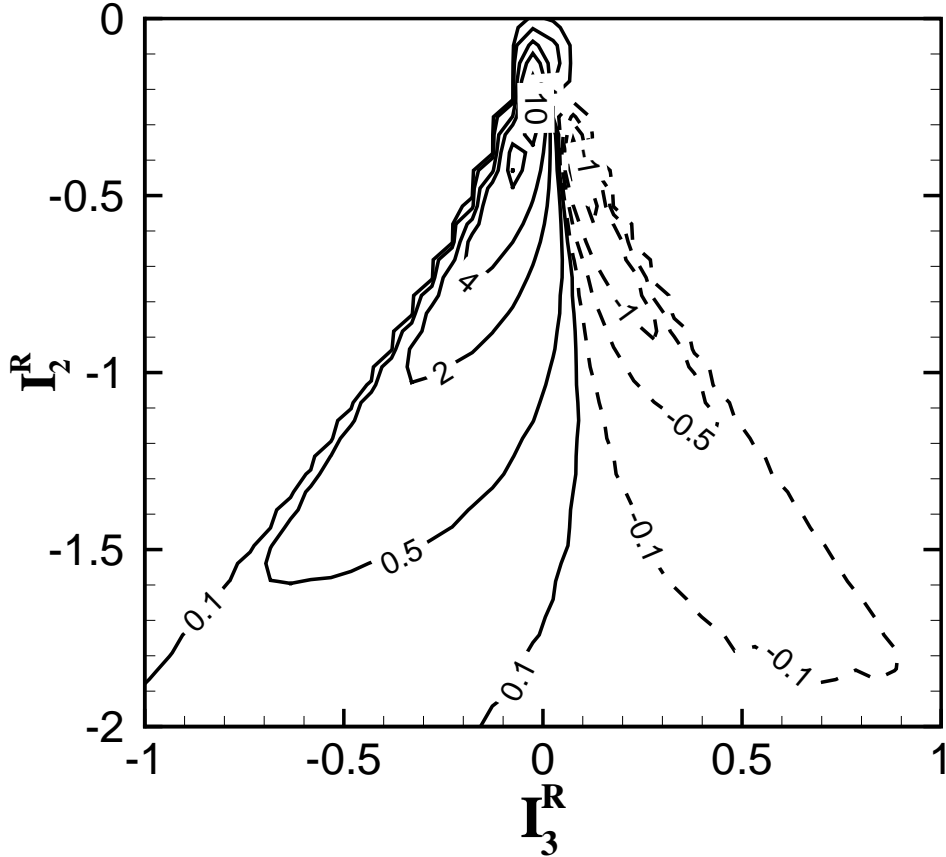


FIG. 17: The weighted conditional average of the SGS helicity dissipation in helical turbulence:  $P(\mathbf{I}_3^R, \mathbf{I}_2^R) \langle \Pi_H | \mathbf{I}_3^R, \mathbf{I}_2^R \rangle / \langle \Pi_H \rangle$ . Solid lines are for positive contours and dashed for negative.

between  $R^*$  and  $\Pi_H$  in both helical and non-helical data. Second, in helical turbulence, it has higher probabilities to observe positive fluctuations in  $\Pi_H$ , compared with non-helical turbulence. It appears that when  $R^*$  decreases,  $\Pi_H$  becomes more intermittent, with wider probability distributions, but the variation is small.

Figure 20 shows the averages of  $\Pi_H$  conditioned on values of  $R^*$ , weighted with the PDF of  $R^*$ . The inset shows the same conditional averages without weighting. One can see that, interestingly, the conditional mean dissipation tends to be positive when  $R^* < 0$ , and negative when  $R^* > 0$ , in both helical and non-helical turbulence. For non-helical turbulence, the curves are symmetric with respect to the origin. For helical turbulence, the curves are shifted upwards, so as to generate a mean positive SGS helicity dissipation. When  $\Delta = 16\delta x$ , the curve has a maximum at  $R^* = -1$ . Thus the axisymmetric straining structure (of the vortex lines) produces strongest positive SGS helicity dissipation. Strongest negative SGS helicity dissipation comes from structures with  $R^* = 1$ . For  $\Delta = 8\delta x$ , the conditional dissipation

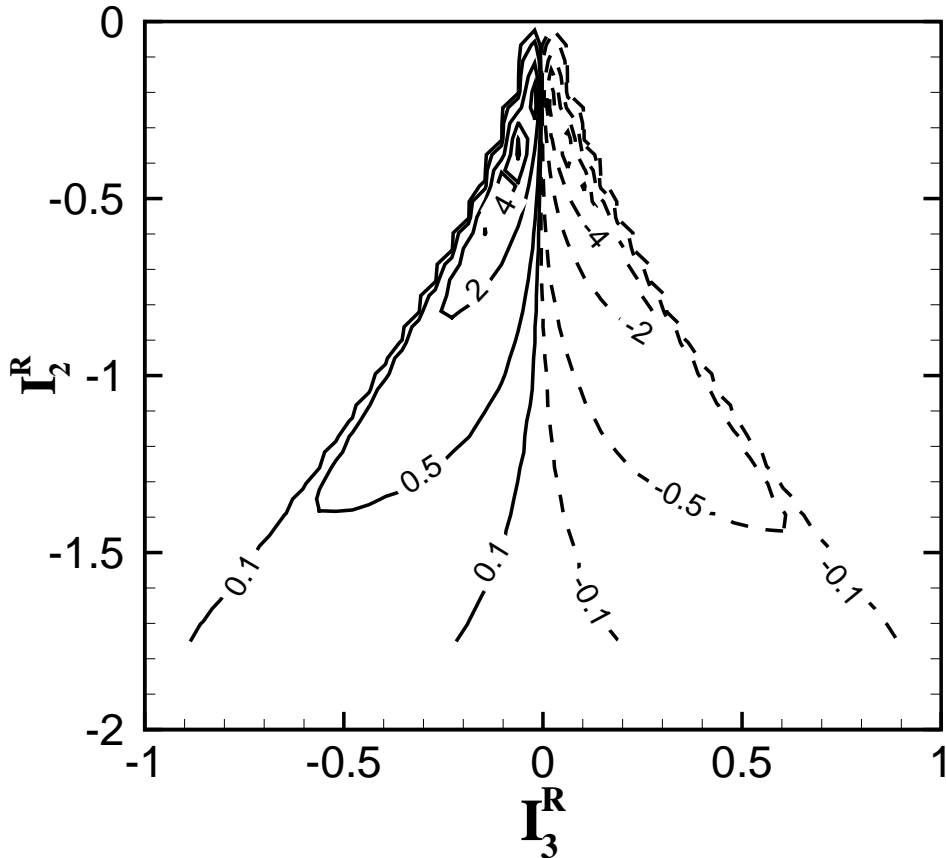


FIG. 18: Same as Figure 17, but for non-helical turbulence.

rate still takes maximum at  $R^* = -1$ , as shown by the dashed line in the inset. But the contribution to the total dissipation is maximum at  $R^* \approx -0.5$ , due to higher probability to observe this value of  $R^*$ .

To summarize the results on the invariants and eigenvalues of  $\tilde{R}_{ij}$ , we observe that, in helical turbulence with positive helicity injection rate, it is more probable to observe negative  $R_\beta$  and events with negative  $\mathbf{I}_3^R$ , especially those around the left Vieillefosse tail. The SGS helicity dissipation fluctuations are negatively correlated with  $R^*$  in both helical and non-helical turbulence. The structures around the Vieillefosse tails in the  $(\mathbf{I}_3^R, \mathbf{I}_2^R)$  phase plane with  $R^* = \pm 1$  contribute important parts to the total SGS helicity dissipation.

#### D. Alignment between tensors and vectors

Past studies on turbulence have found different preferential alignment trends between various tensors and vectors. Examples include the well-known alignment between  $\tilde{\omega}$  and

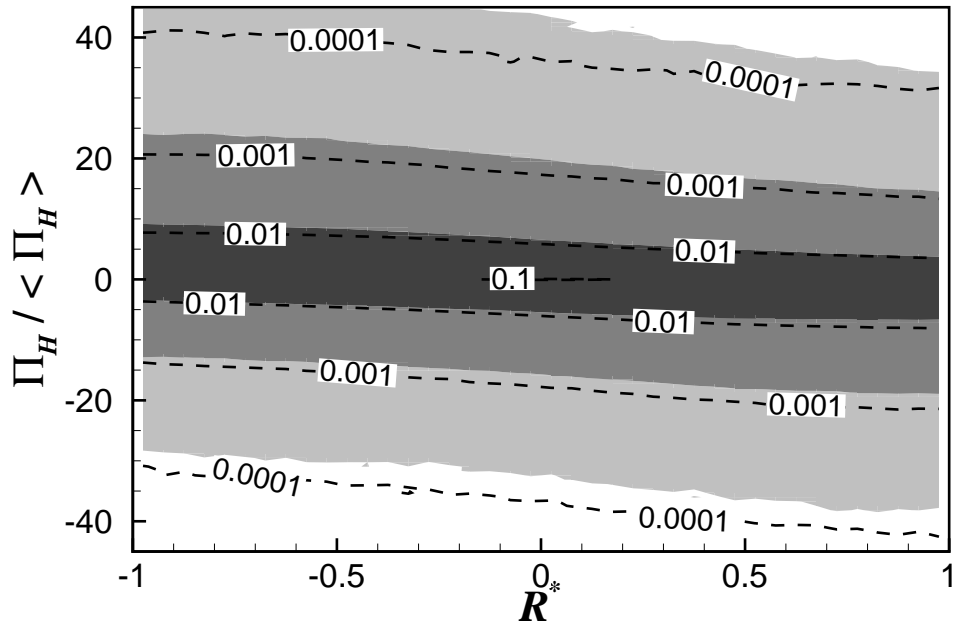


FIG. 19: The joint PDF of  $R^*$  and SGS helicity dissipation  $\Pi_H$ . Gray-scales: helical turbulence; dashed lines: non-helical.  $\Delta = 16\delta x$ .  $\langle \Pi_H \rangle$  is the mean SGS helicity dissipation in helical turbulence.

the intermediate eigenvector of the strain rate tensor [35, 36, 62], the alignment between the SGS stress tensor and the vorticity vector [33, 34], and the alignment between the strain rate tensor and the SGS stress tensor [33]. These geometrical structures are related to the various dynamical processes of turbulence, such as vortex stretching etc [33]. In this section, we will study the alignment between the vorticity strain rate  $\tilde{R}_{ij}$  and the vorticity vector  $\tilde{\omega}$  and vector  $\tilde{\xi}$ . The results will provide useful insight into the local structure of the vorticity field. In the results to be presented in the rest of this paper, we often observe only small differences between helical and non-helical turbulence. Therefore only results in helical turbulence will be presented unless stated otherwise.

The alignment between  $\tilde{R}_{ij}$  and  $\tilde{\xi}$  is characterized by the relative angles between the eigenvectors  $\mathbf{R}_i (i = \alpha, \beta, \gamma)$  and  $\tilde{\xi}$ , denoted as  $\theta_i$ . Figure 21 plots the PDFs of  $|\cos \theta_i| \equiv |\tilde{\xi} \cdot \mathbf{R}_i|/|\tilde{\xi}|$  at several different filter scales. Interestingly, we observe that the PDFs for  $\mathbf{R}_\beta$  show a very strong peak at  $|\cos \theta_i| = 1$ , implying that there is a high probability for  $\tilde{\xi}$  to align with the intermediate eigenvector  $\mathbf{R}_\beta$ . The peaks are reduced only slightly when  $\Delta$  increases. The distributions for  $\mathbf{R}_\alpha$  and  $\mathbf{R}_\gamma$  are very close to each other. At small scales, both have peaks at  $|\cos \theta_i| = 0$ , showing that  $\tilde{\xi}$  tends to be perpendicular to both  $\mathbf{R}_\alpha$  and  $\mathbf{R}_\gamma$ . When the filter scale increases, the peaks weaken. Note that, the same PDFs in a

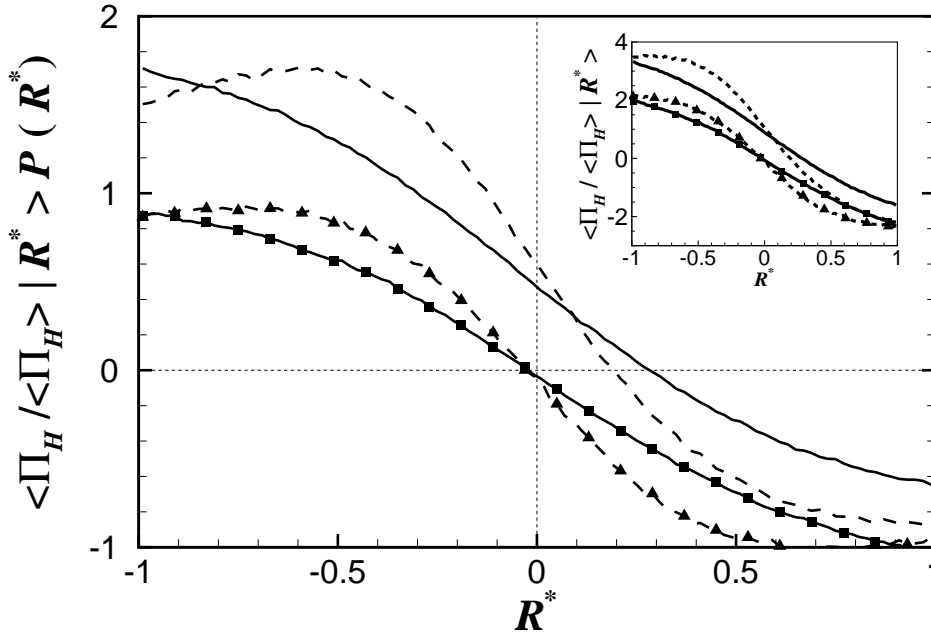


FIG. 20: The conditional averages of the SGS helicity dissipation, weighted by the PDF of  $R^*$ , as functions of  $R^*$ . Lines: helical turbulence; symbols with lines: non-helical turbulence. Solid line and squares:  $\Delta = 16\delta x$ ; dashed line and triangles:  $\Delta = 8\delta x$ . Inset shows the conditional averages without weighting.

Gaussian field with same energy and helicity spectra are uniform for all the eigenvectors. Thus, the peaks observed in the Figure 21 are the consequence of the non-trivial vortex structures in turbulence.

The origin of the preferred  $\tilde{\xi} - \tilde{R}_{ij}$  alignment and its dynamical consequences are not yet clear. Here we only comment that, the closeness between the results for  $\mathbf{R}_\alpha$  and  $\mathbf{R}_\gamma$ , observed in Figure 21, is a consequence of reflectional symmetry. As  $\tilde{R}_{ij}$  is a pseudo-tensor, its eigenvalues are pseudo-scalars, and have opposite signs in the mirror image of the flow field. By the ordering of the eigenvalues, the largest eigenvalue in the mirror flow field is thus  $-R_\gamma$ , the smallest one is  $-R_\alpha$ . In a reflectionally symmetric flow field, the statistics is invariant upon a reflectional transformation. In particular, the statistics of the largest eigenvalue should stay the same. Therefore, the PDF of  $|\tilde{\xi} \cdot \mathbf{R}_\alpha|/|\tilde{\xi}|$  should be the same as that of  $|\tilde{\xi} \cdot (-\mathbf{R}_\gamma)|/|\tilde{\xi}| = |\tilde{\xi} \cdot \mathbf{R}_\gamma|/|\tilde{\xi}|$  in a reflectionally symmetric flow field. In non-helical turbulence we indeed find that the PDFs for  $\mathbf{R}_\alpha$  and  $\mathbf{R}_\gamma$  are the same (not shown). In helical turbulence, there is also only small difference between the two PDFs, as is seen in Figure 21.

The PDFs for the alignment between  $\tilde{R}_{ij}$  and  $\tilde{\omega}$  in helical turbulence are presented in Figure 22. The lines are for  $\Delta = 16\delta x$  and the symbols are for  $\Delta = 8\delta x$ . For  $\Delta = 16\delta x$ ,

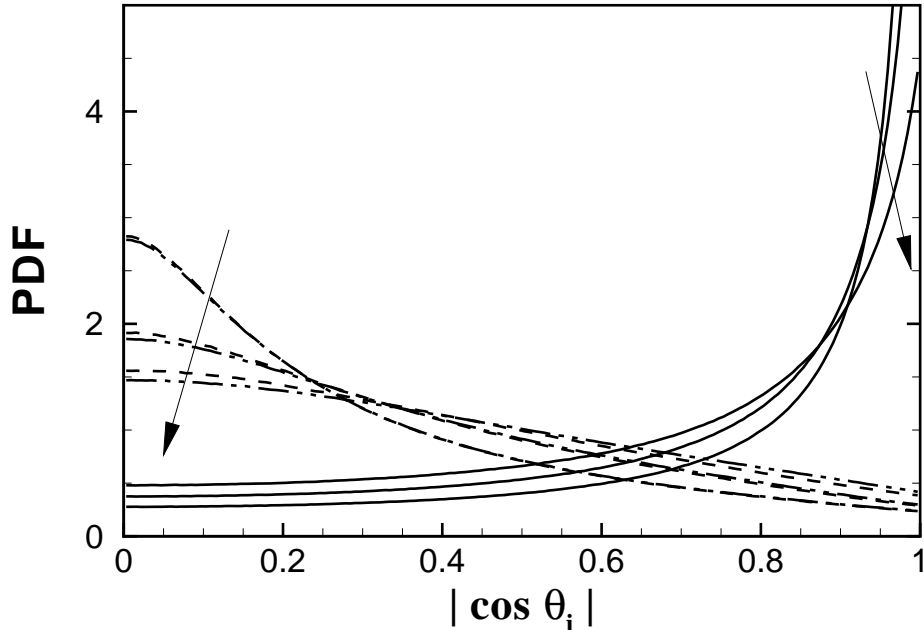


FIG. 21: PDFs of  $|\cos \theta_i| \equiv |\tilde{\boldsymbol{\xi}} \cdot \mathbf{R}_i|/|\tilde{\boldsymbol{\xi}}|$ , where  $\mathbf{R}_i$  ( $i = \alpha, \beta, \gamma$ ) is the eigenvector of  $\tilde{R}_{ij}$ , at  $\Delta = 16\delta x, 8\delta x, 0\delta x$ . Dashed lines:  $i = \alpha$ ; solid:  $\beta$ ; dash-double-dotted:  $\gamma$ .  $\Delta$  increases along the directions of the arrows.

we observe that the PDFs for  $\mathbf{R}_\alpha$  and  $\mathbf{R}_\gamma$  are almost the same. Both peak at  $\cos \theta \approx 0.71$  corresponding to  $\theta \approx 45^\circ$ . Thus, the vorticity vector tends to take approximately  $45^\circ$  angles with  $\mathbf{R}_\alpha$  and  $\mathbf{R}_\gamma$  and tilts slightly towards the former. On the other hand, the PDF of  $\mathbf{R}_\beta$  reaches maximum at zero, although the peak is not sharp. In other words,  $\tilde{\boldsymbol{\omega}}$  and  $\mathbf{R}_\beta$  prefer to be perpendicular to each other, but with high probabilities to make other angles. When  $\Delta = 8\delta x$ , the peaks in the PDFs for  $\mathbf{R}_\alpha$  and  $\mathbf{R}_\gamma$  become stronger, and are also reached at  $\theta \approx 45^\circ$ .

The  $45^\circ$  angle observed in Figure 22, which is also observed in non-helical turbulence, suggests that it may come from some simple flow structures. Recall that in a uniform two-dimensional shear layer (see Figure 23(a)), the eigenvectors corresponding to the two non-zero eigenvalues of the strain rate tensor will make  $45^\circ$  with the velocity vector. Similarly, for a two-dimensional vortex layer with uniform transverse gradient, as illustrated in Figure 23(b), the two eigenvectors  $\mathbf{R}_\alpha$  and  $\mathbf{R}_\gamma$  make  $45^\circ$  with the vorticity vector itself. This observation suggests that the preferred angle of  $45^\circ$  observed in Figure 22 may be related to such layer-like structures. More generally, one expects to observe preferential  $45^\circ$  alignments between  $\tilde{\boldsymbol{\omega}}$  and  $\mathbf{R}_\alpha$  and  $\mathbf{R}_\gamma$  as long as the gradient of vorticity along a perpendicular direction is much stronger than the gradient along other directions. In particular, this may include both

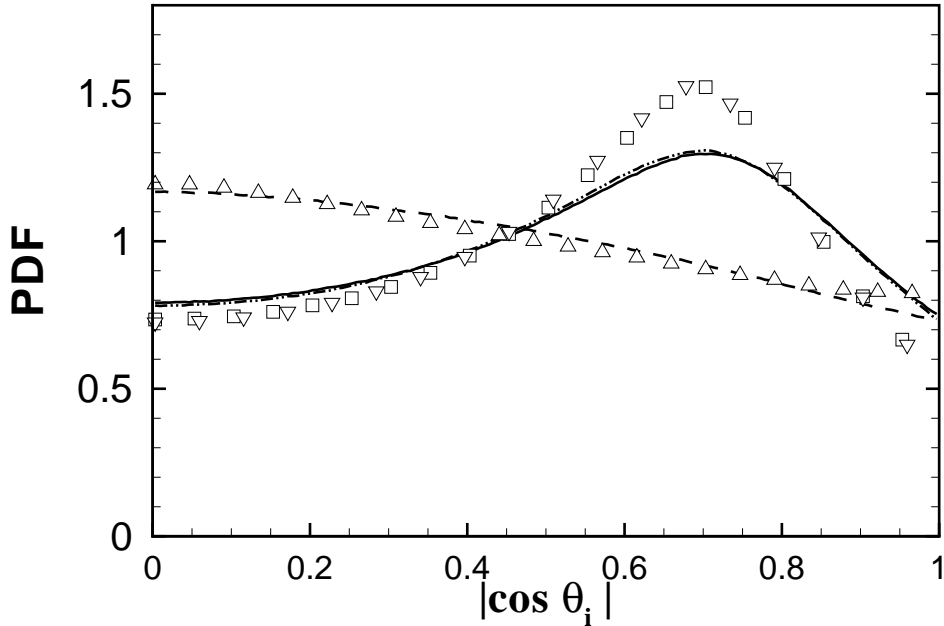


FIG. 22: PDF of  $|\cos \theta_i| \equiv |\tilde{\omega} \cdot \mathbf{R}_i|/|\tilde{\omega}|$ , where  $\theta_i$  is the angle between  $\tilde{\omega}$  and eigenvector  $\mathbf{R}_i$  ( $i = \alpha, \beta, \gamma$ ). Lines:  $\Delta = 16\delta x$ ; symbols:  $\Delta = 8\delta x$ . Solid line and squares:  $\mathbf{R}_\alpha$ ; dashed line and deltas:  $\mathbf{R}_\beta$ ; dash-double-dotted line and gradients:  $\mathbf{R}_\gamma$ .

vortex tubes and vortex sheets (see, e.g., [34, 63]).

The alignment between  $\tilde{\omega}$  and the eigenvectors of  $\tilde{R}_{ij}$  is correlated with the SGS helicity dissipation. Figure 24 plots the PDFs of  $|\cos \theta_i|$  conditioned on  $\Pi_H > 0$  (lines) and  $\Pi_H < 0$  (symbols), i.e.,  $P(|\cos \theta_i| | \Pi_H > 0)$  and  $P(|\cos \theta_i| | \Pi_H < 0)$  ( $i = \alpha, \beta, \gamma$ ). Comparing with Figure 22, one can find that, when conditioned on positive  $\Pi_H$ , the differences between the curves for  $\mathbf{R}_\alpha$  and  $\mathbf{R}_\gamma$  are amplified.  $P(|\cos \theta_\alpha| | \Pi_H > 0)$  is shifted to the right with a peak at  $\cos \theta_\alpha \approx 0.77$ , while  $P(|\cos \theta_\gamma| | \Pi_H > 0)$  is shifted to the left and peaks at  $\cos \theta_\gamma \approx 0.52$ . The results imply that  $\tilde{\omega}$  becomes more aligned with  $\mathbf{R}_\alpha$  in regions with higher SGS helicity dissipation. When conditioned on negative  $\Pi_H$ , the trends reverse. That is, the peak of  $P(|\cos \theta_\alpha| | \Pi_H < 0)$  now moves to the left. The whole curve is close to  $P(|\cos \theta_\gamma| | \Pi_H > 0)$ . The curve for  $\mathbf{R}_\gamma$  moves to the right and peaks at approximately the same location as  $P(|\cos \theta_\alpha| | \Pi_H > 0)$ , whilst the peak value is a bit higher. The PDFs corresponding to  $\mathbf{R}_\beta$  show only small changes upon the conditioning.

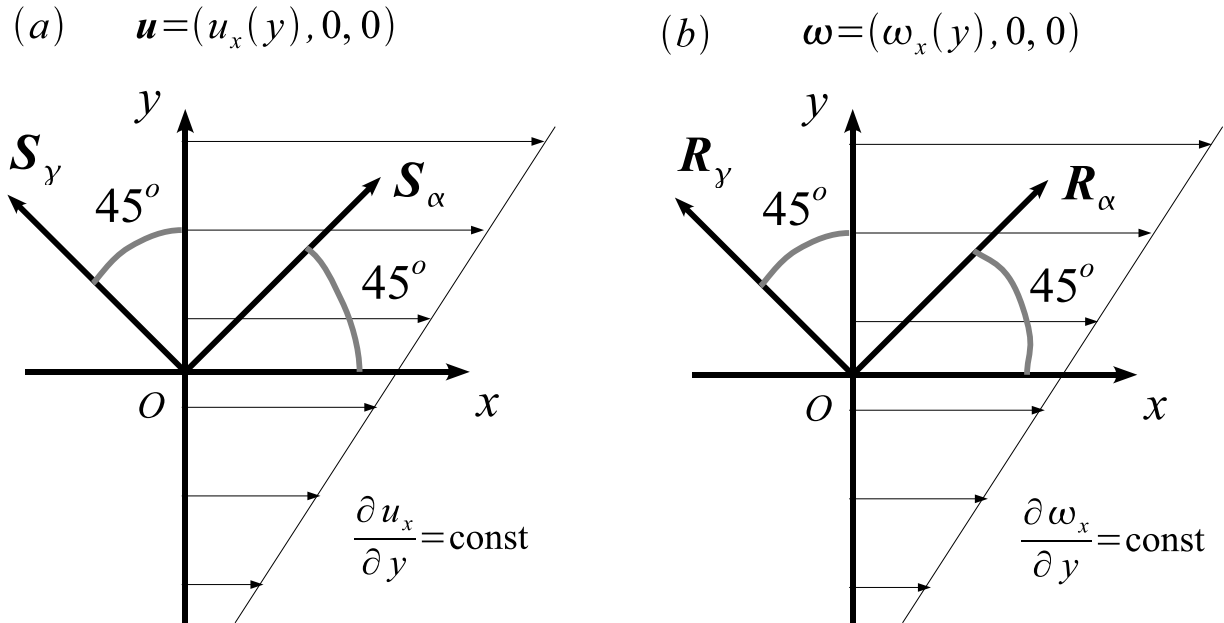


FIG. 23: Alignment trends in (a) a homogeneous shear flow, and (b) a vortex sheet with unidirectional vorticity and uniform transverse gradient.

### E. Alignment trends between tensors

In this subsection, we consider the alignment trends between  $\tilde{R}_{ij}$  and the (minus) SGS stress tensor  $-\tau_{ij}$  and other related tensors. As is shown by Eq. (10), nine inner products can be defined out of the six eigenvectors of the two tensors. However, they are not all independent and only three angles are needed to specify the relative orientation of the two eigen-frames. We use the three angles  $(\theta, \phi, \zeta)$  defined in [33], also illustrated in Figure 25. Specifically,  $\theta$  is defined as the angle between  $\mathbf{R}_\alpha$  and  $(-\boldsymbol{\tau})_\alpha$ .  $\phi$  is the angle between  $\mathbf{R}_\beta$  and the projection of  $(-\boldsymbol{\tau})_\alpha$  on the  $\mathbf{R}_\beta - \mathbf{R}_\gamma$  plane.  $\zeta$  is the angle between the projection of  $\mathbf{R}_\gamma$  on the  $(-\boldsymbol{\tau})_\beta - (-\boldsymbol{\tau})_\gamma$  plane, denoted by  $\mathbf{R}_\gamma^P$ , and  $(-\boldsymbol{\tau})_\gamma$ . Because the eigenvectors are determined only up to an arbitrary constant, which can be either positive or negative, the range of each angle is  $[0, 90^\circ]$ . In a Gaussian velocity field, the joint PDF  $P(\cos \theta, \phi, \zeta)$  is approximately uniform.

We first consider the alignment between  $\tilde{R}_{ij}$  and  $-\tau_{ij}$ . Figure 26 shows several slices cutting through the 3-dimensional (3D) joint PDF  $P(\cos \theta, \phi, \zeta)$ , evaluated at filter scale  $\Delta = 16\delta x$ . As one can see, the distribution has a peak with approximate value 1.37, approximately located at  $(\cos \theta, \phi, \zeta) = (0.71, 1.55, 1.55)$ , corresponding to angles  $(\theta, \phi, \zeta) \approx (45^\circ, 90^\circ, 90^\circ)$ . The same PDF calculated from the non-helical turbulence data is plotted in

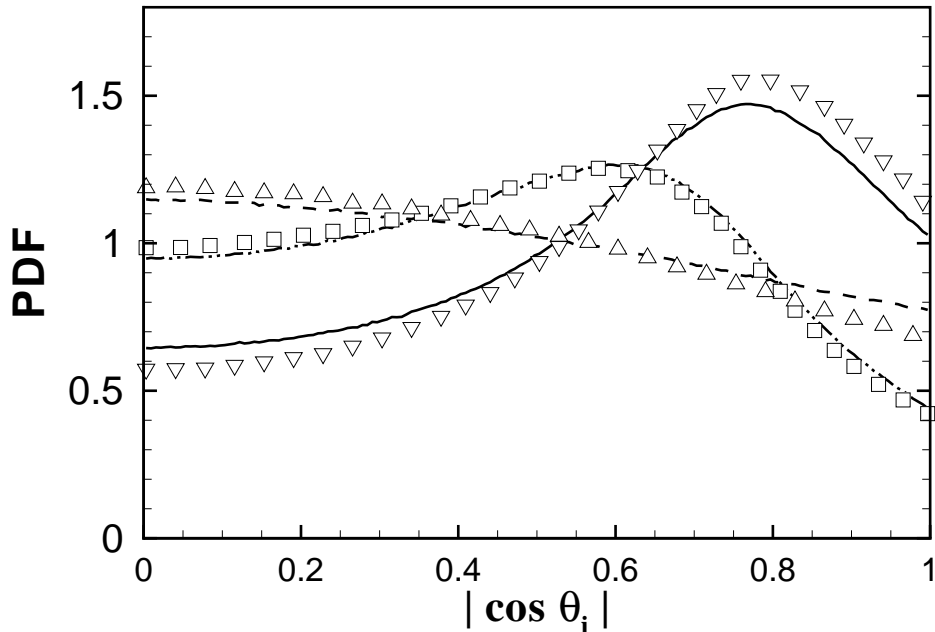


FIG. 24: Conditional PDFs of  $|\cos \theta_i| \equiv |\tilde{\omega} \cdot \mathbf{R}_i|/|\tilde{\omega}|$ ,  $i = \alpha, \beta, \gamma$ . Lines: conditioned on positive  $\Pi_H$ ; symbols: conditioned on negative  $\Pi_H$ . Solid line and squares:  $i = \alpha$ ; dashed line and deltas:  $i = \beta$ ; dash-double-dotted line and gradients:  $i = \gamma$ .  $\Delta = 16\delta x$ .

Figure 27. Interestingly, we again observe a peak at approximately the same location, but slightly shifted towards smaller values of  $\cos \theta$ . The peak value is about 1.35. Thus, the peak configuration is a trend existing in both helical and non-helical turbulence.

We will make a connection between this alignment trend with the  $\tilde{\omega} - \tilde{R}_{ij}$  alignment we presented above, and the  $\tilde{\omega} - \tau_{ij}$  alignment reported in [34]. First, the peak configuration in the above distributions is graphically illustrated in Figure 28. In this configuration  $(-\boldsymbol{\tau})_\gamma$  aligns with  $\mathbf{R}_\beta$ , while  $(-\boldsymbol{\tau})_\alpha$  and  $(-\boldsymbol{\tau})_\beta$  both make an angle of  $45^\circ$  with  $\mathbf{R}_\alpha$ . Second, let us recall the results concerning the alignment between  $\tilde{\omega}$  and  $\tau_{ij}$ . As is shown in [34], there are high probabilities for  $\tilde{\omega}$  to align with  $(-\boldsymbol{\tau})_\alpha$  and  $(-\boldsymbol{\tau})_\beta$ . These alignment trends are reproduced in our helical turbulence data, given in Figure 29. Plotted in Figure 29 are the PDFs of  $|\cos \theta_i| \equiv |\tilde{\omega} \cdot (-\boldsymbol{\tau})_i|/|\tilde{\omega}|$  ( $i = \alpha, \beta, \gamma$ ), where  $\theta_i$  is the angle between  $\tilde{\omega}$  and the  $i$ th eigenvector of  $-\tau_{ij}$ . One indeed finds sharp peaks at 1 for  $(-\boldsymbol{\tau})_\alpha$  and  $(-\boldsymbol{\tau})_\beta$ , which are plotted with solid and dashed lines. For  $(-\boldsymbol{\tau})_\gamma$ , the PDF also has a rather strong maximum at the origin, implying that  $\tilde{\omega}$  tends to be perpendicular to  $(-\boldsymbol{\tau})_\gamma$ . Finally, the  $\tilde{\omega} - \tilde{R}_{ij}$  alignment trends have been shown in Figure 22, in which we find  $\tilde{\omega}$  tends to make  $45^\circ$  with both  $\mathbf{R}_\alpha$  and  $\mathbf{R}_\gamma$ , and be perpendicular to  $\mathbf{R}_\beta$ . Therefore, it is not difficult to see that, if the two most probable  $\tilde{\omega} - \tilde{R}_{ij}$  and  $\tilde{\omega} - \tau_{ij}$  alignments take place at the same time, one

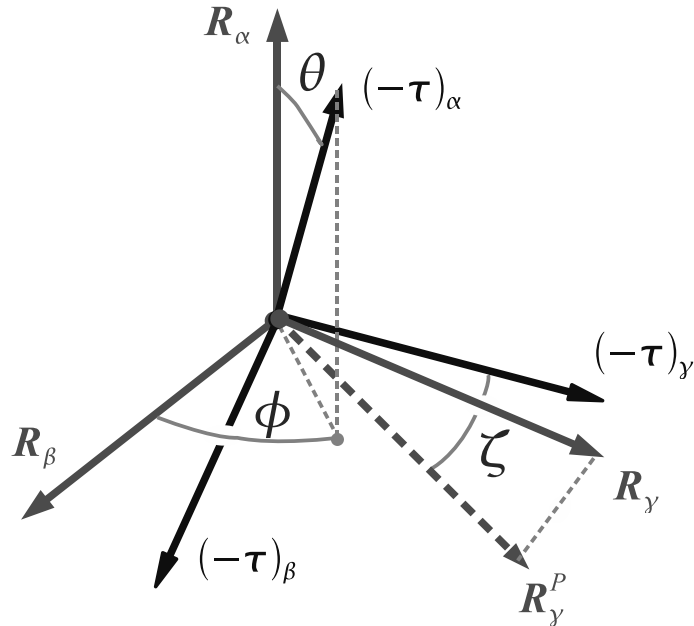


FIG. 25: The angles  $(\theta, \phi, \zeta)$  defining the relative orientation between the eigen-frames of tensors  $\tilde{R}_{ij}$  and  $-\tau_{ij}$ .

would observe the peak  $\tilde{R}_{ij} - \tau_{ij}$  alignment shown in Figure 28. Thus, the observed  $\tilde{R}_{ij} - \tau_{ij}$  alignment is consistent with previous results. The argument suggests the pivotal role of vorticity in inducing various geometrical alignments in turbulence.

As already noted, there are some differences between helical and non-helical turbulence in the three-dimensional joint PDF distributions of  $(\cos\theta, \phi, \zeta)$ . To get a clear look at the differences, we consider the marginal distributions  $P(\cos\theta)$ ,  $P(\phi)$ , and  $P(\zeta)$ . Figure 30 shows the marginal distributions for both helical and non-helical data, with solid and open symbols, respectively. For comparison, the same results for a Gaussian velocity field with same energy and helicity spectra are also shown with lines. The first observation is that the biggest difference between helical and non-helical turbulence is observed in  $P(\cos\theta)$  (squares). In helical turbulence, the probability to observe larger values for  $\cos\theta$  is substantially higher than in non-helical turbulence, implying that  $(-\tau)_\alpha$  tends to align with  $\mathbf{R}_\alpha$  closer in helical turbulence. We can qualitatively understand the effects of this difference on the magnitude of SGS helicity dissipation via Eq. (10). Let's focus on the first term in the equation. By definition  $R_\alpha$  and  $(-\tau)_\alpha$  are positive. Also,  $\mathbf{R}_\alpha \cdot (-\tau)_\alpha \equiv \cos\theta$  according to our definition of angle  $\theta$ . As a result, the first term in Eq. (10) is positive and increases with  $\cos\theta$ . Thus, Figure 30 implies that, in helical turbulence, this term tends to generate larger values of positive helicity dissipation. For the distribution of  $\phi$ , both helical and non-helical turbulence

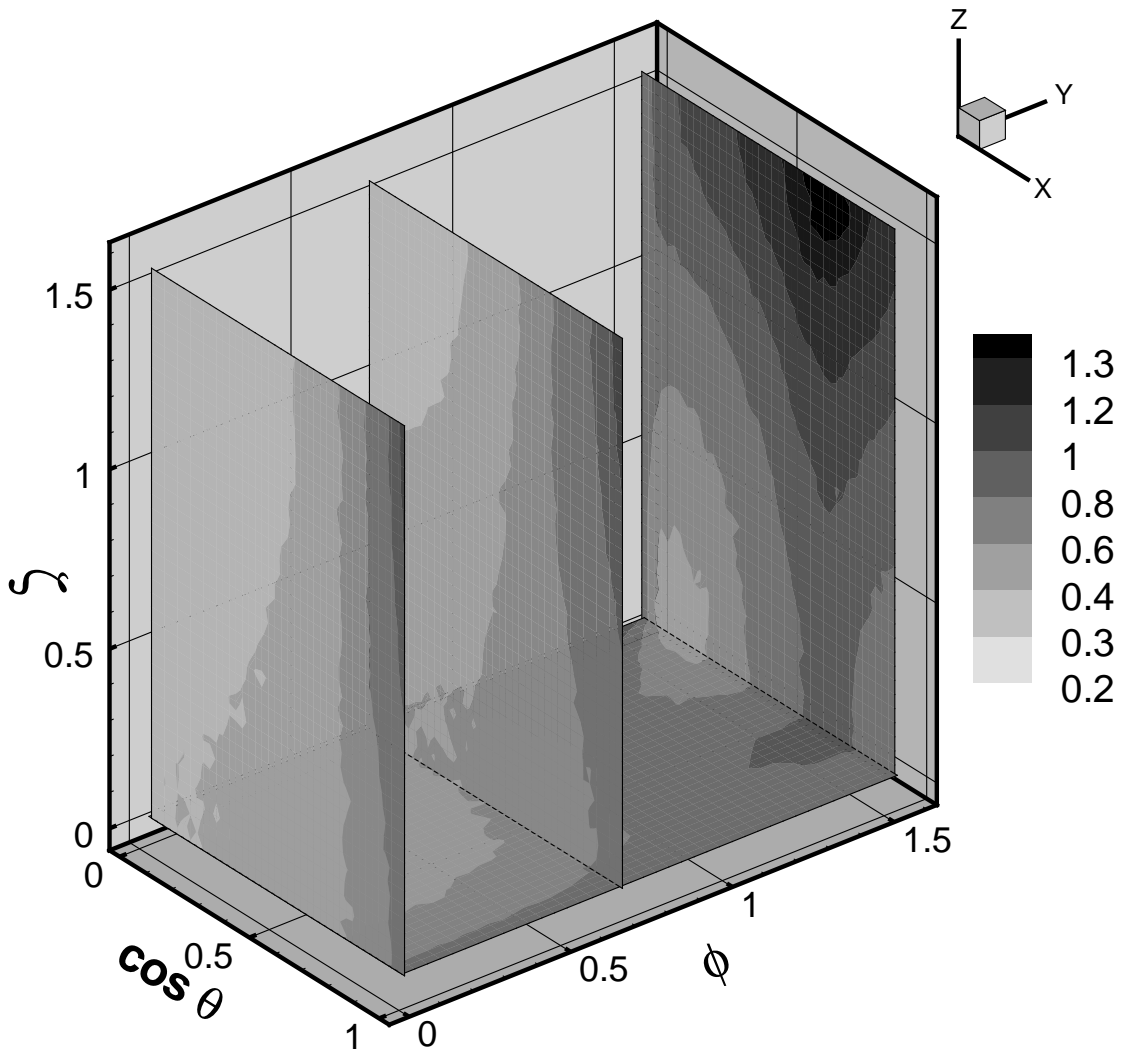


FIG. 26: Joint PDF  $P(\cos \theta, \phi, \zeta)$  in helical DNS for  $\tilde{R}_{ij}$  and  $\tau_{ij}$ .  $\Delta = 16\delta x$ .

show higher probabilities to observe larger values (values close to  $\pi/2$ ), compared with the Gaussian field. The probability to find  $\phi$  near  $\pi/2$  is slightly higher in non-helical data than in the helical one. Finally, the distributions of  $\zeta$  in either helical or non-helical turbulence are quite close to that in the Gaussian field, and is nearly uniform over the interval  $[0, \pi/2]$ .

We next consider the dependence of the  $\tilde{R}_{ij} - \tau_{ij}$  alignment on SGS helicity dissipation  $\Pi_H$ , in terms of the PDFs of the angles conditioned on the values of  $\Pi_H$ . The conditional PDFs of  $\cos \theta$  are plotted in Figure 31, with the unconditional one shown with a dotted line for comparison. Four different conditions are considered:  $\Pi_H > 2\langle \Pi_H \rangle$ ,  $\Pi_H > 0$ ,  $\Pi_H < 0$ , and  $\Pi_H < -2\langle \Pi_H \rangle$ . It can be seen that the probabilities for larger values of  $\cos \theta$  are increased dramatically when conditioned on positive  $\Pi_H$  (solid squares), and decreased

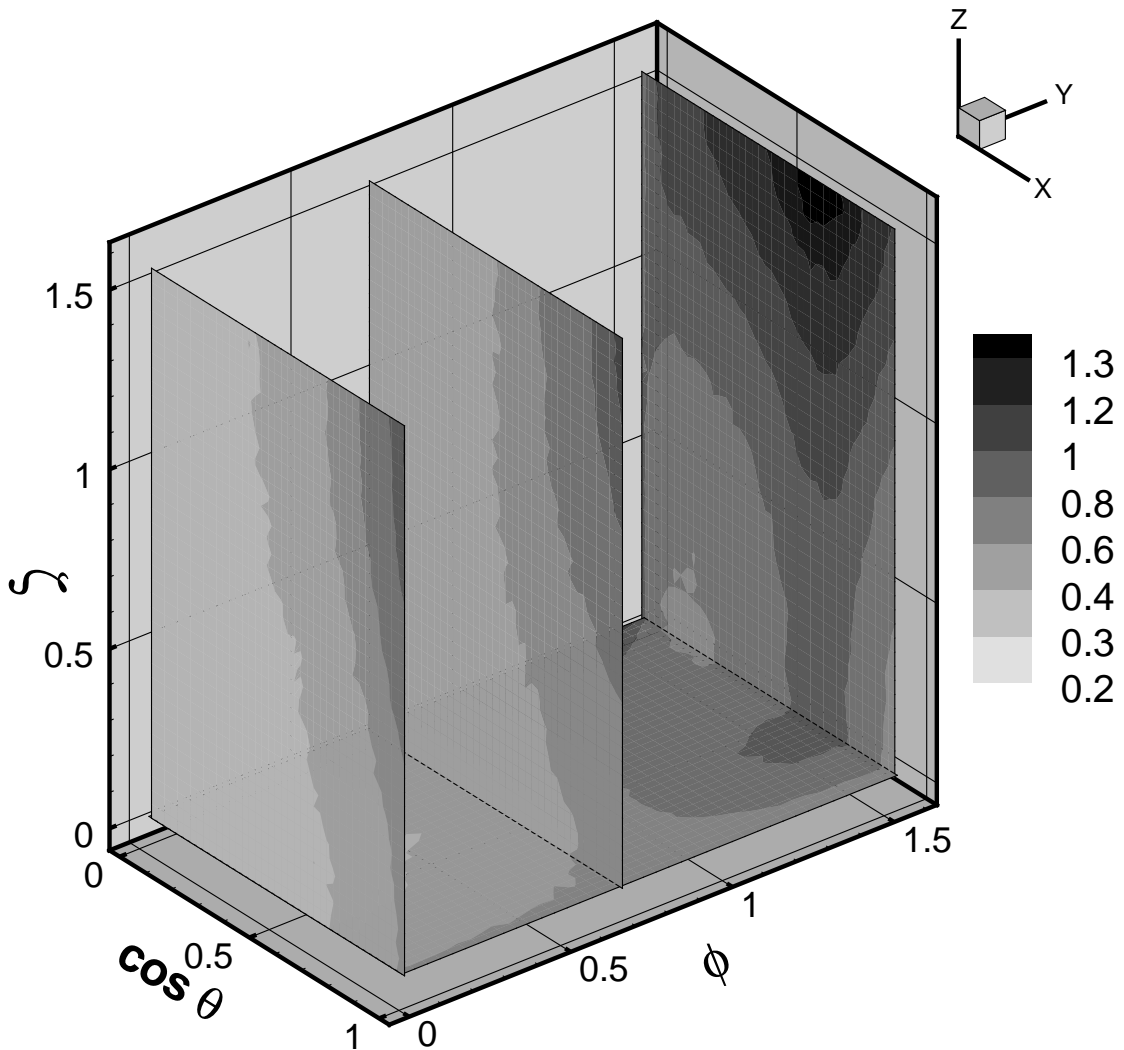


FIG. 27: Joint PDF  $P(\cos \theta, \phi, \zeta)$  in non-helical DNS for  $\tilde{R}_{ij}$  and  $\tau_{ij}$ .  $\Delta = 16\delta x$ .

when conditioned on negative ones (open squares). The changes are further enhanced when conditioned on large magnitude fluctuations  $\Pi_H > 2\langle\Pi_H\rangle$  and  $\Pi_H < -2\langle\Pi_H\rangle$  (circles). Thus, it is more probable to observe closer alignment between  $\mathbf{R}_\alpha$  and  $(-\boldsymbol{\tau})_\alpha$  in regions with larger  $\Pi_H$ , and vice versa.

The amplitude of the changes indicates the sensitiveness of the sign of  $\Pi_H$  on  $\mathbf{R}_\alpha - (-\boldsymbol{\tau})_\alpha$  alignment, which suggests the dominant role of the latter in determining the value of  $\Pi_H$ . If we examine the figure further, we notice that the curves cross over each other at  $\cos \theta \approx 0.7$ , corresponding approximately to  $\theta = 45^\circ$ . Simple calculation shows that, when  $\Pi_H < 0$ , the probability for  $\cos \theta > 0.7$  equals approximately 0.15 and that for  $\cos \theta < 0.7$  is 0.85. When  $\Pi_H > 0$ , the probability to find  $\cos \theta > 0.7$  is about 0.53. The latter can be compared with

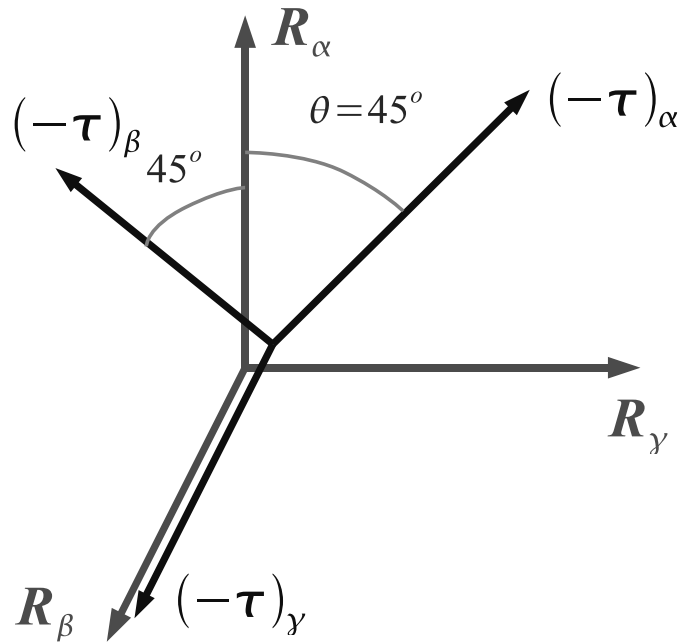


FIG. 28: The configuration of eigenframes for  $\tilde{R}_{ij}$  and  $\tau_{ij}$  corresponding to the peak probability density.

the probability 0.42 calculated from the unconditional PDF and 0.33 from the Gaussian field. Thus, regions with negative SGS helicity dissipation are mostly contained in regions with  $\theta > 45^\circ$ . Regions with positive dissipation is more probable to have an angle  $\theta < 45^\circ$ , but configurations with  $\theta > 45^\circ$  also happen rather frequently.

The PDFs for  $\phi$  and  $\zeta$ , plotted in Figures 32 and 33, also show rather strong dependence on SGS helicity dissipation. The PDFs for  $\phi$  become nearly uniform when conditioned on positive  $\Pi_H$ . Recall that  $(-\boldsymbol{\tau})_\alpha$  tends to align more closely with  $\mathbf{R}_\alpha$  when conditioned on larger  $\Pi_H$  (see Figure 31), therefore small fluctuations in the direction of  $(-\boldsymbol{\tau})_\alpha$  can generate large fluctuations in  $\phi$ . This may explain the changes in the PDF of  $\phi$ . On the other hand, when conditioned on  $\Pi_H < 0$  or  $\Pi_H < -2\langle\Pi_H\rangle$ , the probability for  $\phi \approx 90^\circ$  increase significantly, implying that  $(-\boldsymbol{\tau})_\alpha$  is more likely to be perpendicular to  $\mathbf{R}_\beta$  in the regions with negative SGS helicity dissipation. For  $\zeta$ , when conditioned on  $\Pi_H > 0$ , smaller values become more probable, and when conditioned on negative  $\Pi_H$ , it becomes more probable to take larger values.

The SGS helicity dissipation conditioned on the alignment  $(\cos\theta, \phi, \zeta)$  is plotted in Figure 34 for helical data. The distributions are weighted by the joint PDF of  $\cos\theta, \phi$ , and  $\zeta$ , and normalized by the mean SGS helicity dissipation in helical turbulence. In Figure 34, the largest values are observed mostly around  $\cos\theta = 1$ , and rather evenly distributed for

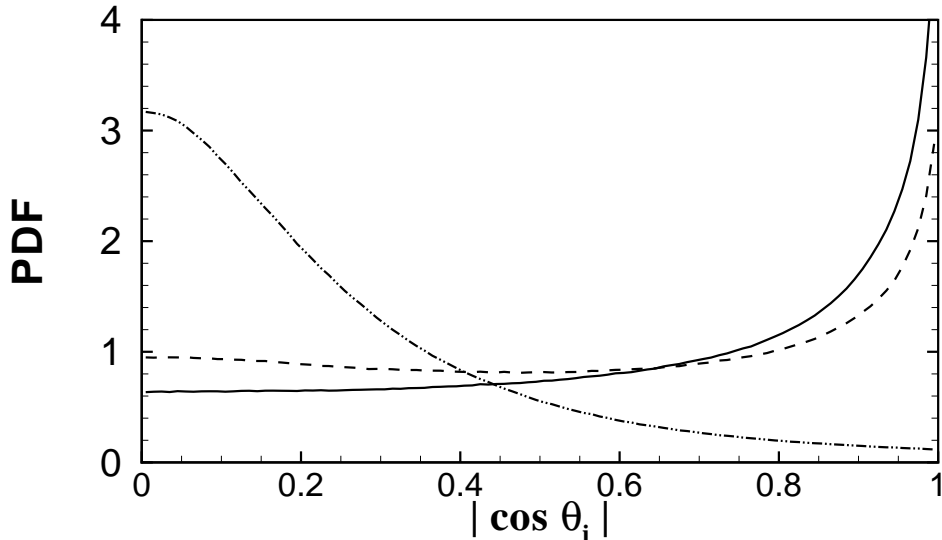


FIG. 29: PDFs of  $|\cos \theta_i| \equiv |\tilde{\omega} \cdot (-\tau)_i|/|\tilde{\omega}|$ , where  $\theta_i$  is the angle between  $\tilde{\omega}$  and the  $i$ th eigenvector  $(-\tau)_i$  of  $-\tau_{ij}$ . Solid line:  $(-\tau)_\alpha$ ; dashed:  $(-\tau)_\beta$ ; dash-double-dotted:  $(-\tau)_\gamma$ .

different values of  $\phi$  and  $\zeta$ . Large negative values are found in the region where  $\theta \lesssim 45^\circ$  with  $\phi$  near  $\pi/2$ . For smaller  $\phi$ , negative values are only observed for larger  $\zeta$ . In general, the figure again shows strong dependence on the  $\mathbf{R}_\alpha - (-\tau)_\alpha$  alignment. Same PDF calculated from non-helical turbulence (not shown) displays similar dependence on the alignment angles, but the magnitudes of positive values are significantly smaller, while the magnitudes of negative values are larger.

Overall, the results show that the value of  $\Pi_H$  depends strongly on  $\cos \theta$ . For example, when  $\phi \approx \pi/2$ , Figure 34 shows that the conditional average changes from positive to negative when  $\cos \theta$  decreases crossing a value around 0.69, corresponding to  $\theta \approx 46^\circ$ . This observation can be partially understood from Eq. (10). Let us focus on the contributions involving the orientation of  $(-\tau)_\alpha$ , consisting of the first three terms in the equation, and denote this part by  $\Pi_{H,\alpha}$ . When  $\phi = \pi/2$ , the expression for  $\Pi_{H,\alpha}$  is reduced to

$$\Pi_{H,\alpha} = (-\tau)_\alpha R_\alpha \cos^2 \theta + (-\tau)_\alpha R_\gamma \sin^2 \theta \quad (21)$$

With  $R_\gamma = -R_\alpha - R_\beta$ , it becomes

$$\Pi_{H,\alpha} = (-\tau)_\alpha R_\alpha \cos 2\theta - (-\tau)_\alpha R_\beta \sin^2 \theta. \quad (22)$$

Since  $R_\alpha > R_\beta$ , the first term is more important. As both  $(-\tau)_\alpha$  and  $R_\alpha$  are positive by definition, the first term increases with  $\cos 2\theta$ , or when  $\theta$  decreases. It is positive when  $\theta < 45^\circ$  and becomes negative when  $\theta > 45^\circ$ . Among the other terms in Eq. (10), it can be

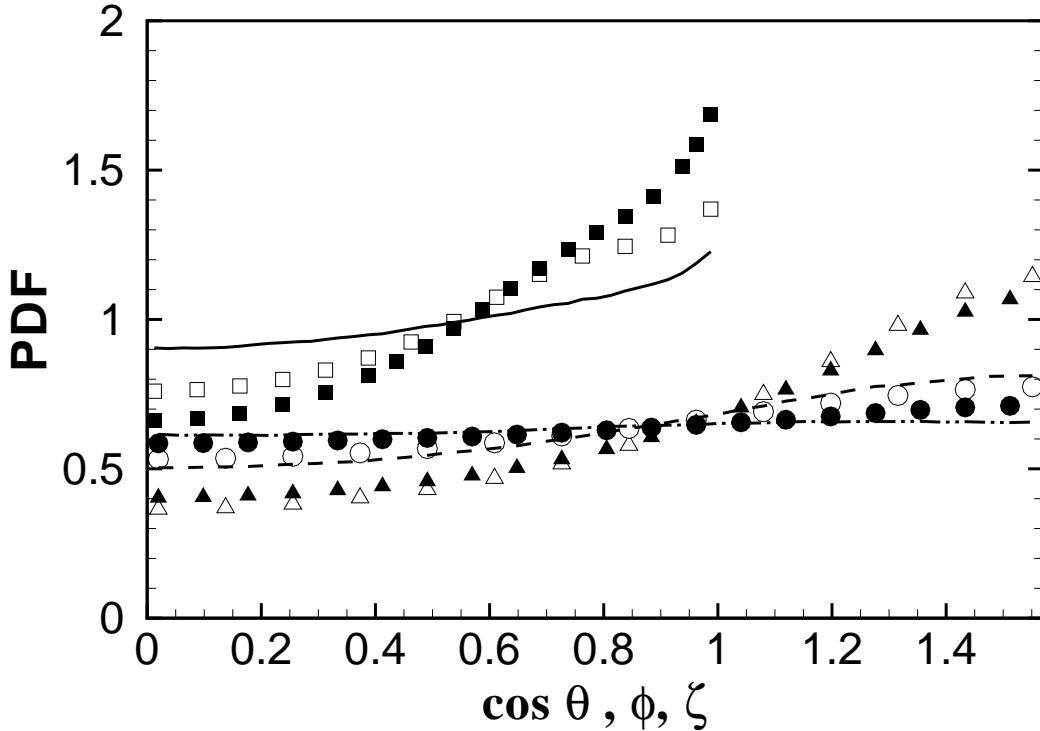


FIG. 30: The marginal PDFs for  $\cos \theta$ ,  $\phi$ , and  $\zeta$ , in helical (solid symbols), non-helical (open symbols) turbulence, and a Gaussian (lines) field. Squares and solid line:  $P(\cos \theta)$ ; deltas and dashed line:  $P(\phi)$ ; circles and dash-double-dotted line:  $P(\zeta)$ .  $\Delta = 16\delta x$ .

shown that the dominant terms also contain the factor  $\cos 2\theta$ . This result thus qualitatively explains the strong dependence on  $\cos \theta$  we see in Figure 34 when  $\phi = \pi/2$ .

For an arbitrary  $\phi$ , the expressions appear too complex for the above analysis to derive meaningful results.

#### IV. CONCLUSIONS

In this paper, we present a study of the geometrical and vortical statistics in the small scales of both helical and non-helical turbulence. We use a filtering approach, in which the helicity flux across different scales is represented by the SGS helicity dissipation. The SGS helicity dissipation is proportional to the product of the SGS stress and the symmetric part of the gradient of the filtered vorticity. Therefore, it is important for the understanding of helicity cascade to examine the local structures of the vorticity field. We thus have focused on the vorticity gradient, the symmetric part of the vorticity gradient, referred to as vorticity strain rate, and the dual vector corresponding to the anti-symmetric part of the vorticity

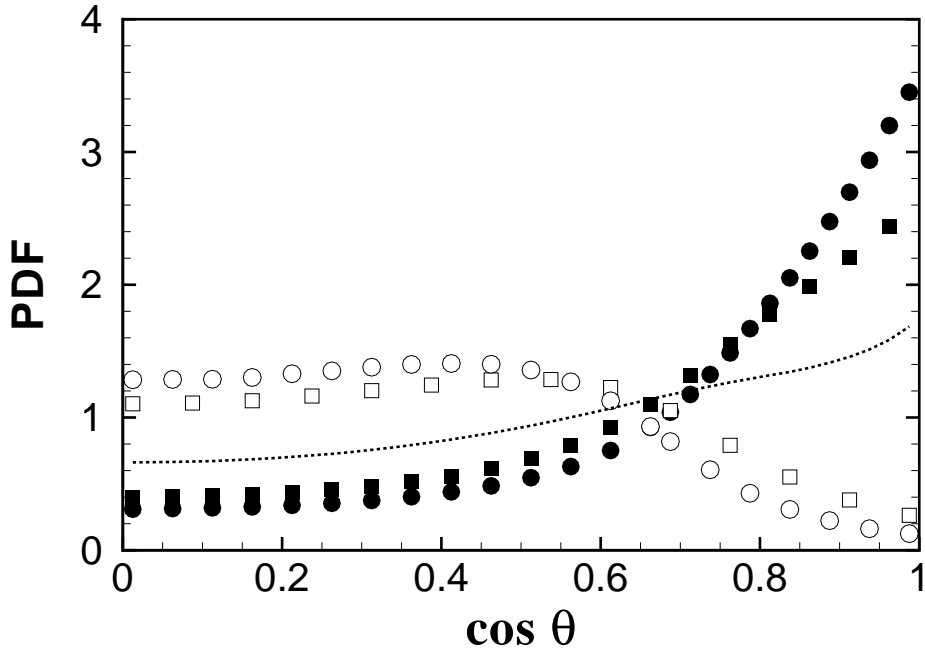


FIG. 31: Conditional PDFs of  $\cos \theta$  in helical turbulence. Solid squares:  $\Pi_H > 0$ ; solid circles:  $\Pi_H > 2\langle \Pi_H \rangle$ ; open squares:  $\Pi_H < 0$ ; open circles:  $\Pi_H < -2\langle \Pi_H \rangle$ . Dotted line is the unconditional PDF shown for comparison.  $\Delta = 16\delta x$ .

gradient. We document the geometrical statistics of these quantities, and their correlation with vorticity, SGS stress, SGS helicity dissipation. Our results can be summarized as follows.

First, a number of geometrical features common to both helical and non-helical turbulence are observed, including the preferred alignment between the dual vector and the intermediate eigenvector of the vorticity strain rate tensor; the preferred  $45^\circ$  alignment between the vorticity vector and both the most contractive and the most extensive eigen-directions of the vorticity strain rate tensor; and the preferred alignment configuration between the vorticity strain rate tensor and the SGS stress tensor. We have shown that, in regions with strong straining of the vortex lines, there is a negative correlation between the fluctuations of the SGS helicity dissipation and the third order tensor invariant of the vorticity gradient tensor. We explain the origin of the correlation as a consequence of the self-induced motions of converging or diverging vortex tubes, which wind up the vortex lines and generate SGS helicity dissipation.

Second, several features unique in helical turbulence are identified. It is found that the joint PDF of the second and third order tensor invariants of the vorticity gradient has an asymmetric distribution, with the direction of skewness depending on the sign of helicity

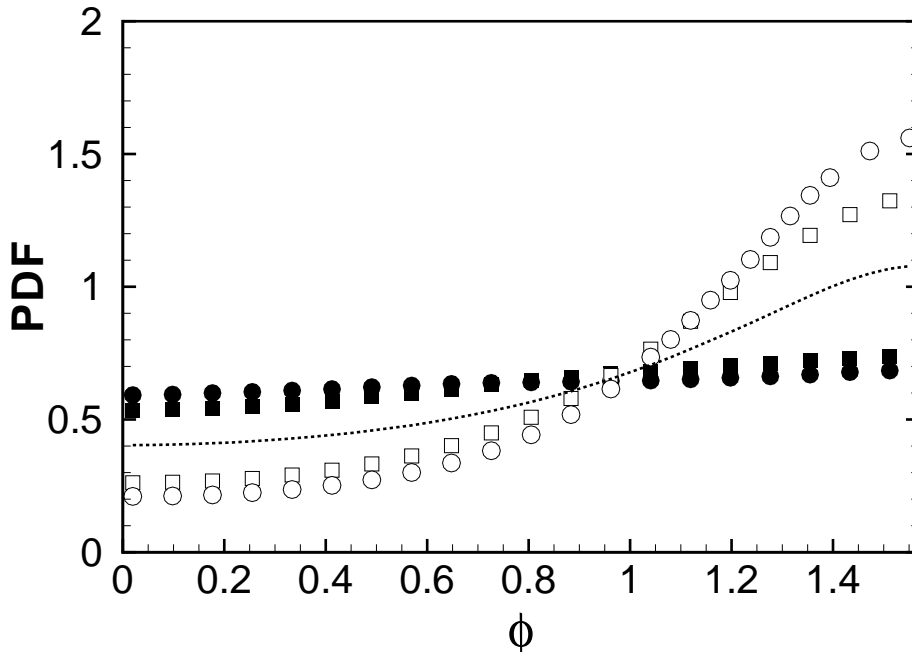


FIG. 32: Same as Figure 31, but for  $\phi$ .

input. Also, we observe that the intermediate eigenvalue of the vorticity strain rate tensor is more probable to take negative values when the helicity injection rate is positive, and vice versa. These features are the main differences between helical and nonhelical turbulence, as far as the geometrical statistics of the vorticity field is concerned. Based on the model of twisted vortex tubes, we show that the asymmetry is dynamically linked to the non-zero mean SGS helicity dissipation in helical turbulence.

In summary, we have observed for the first time a number of interesting geometrical features of the vorticity field in both helical and non-helical turbulence, by looking into the statistics of the gradient of the vorticity. Some of these features have admitted simple dynamical explanations. More work is needed to understand fully the dynamics that generates these features, and to explore their implications. These questions will be the topics of further research.

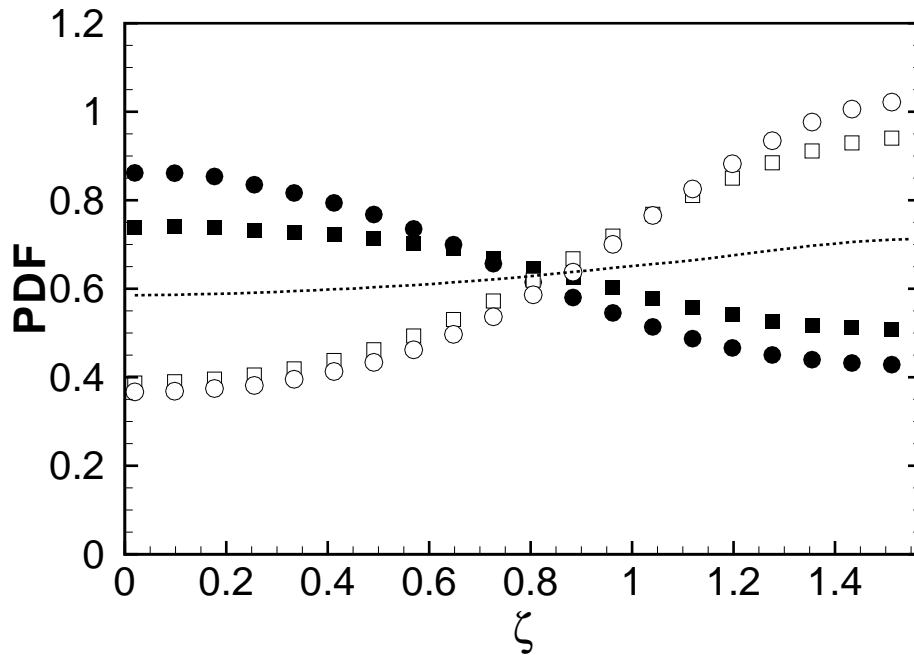


FIG. 33: Same as Figure 31, but for  $\zeta$ .

### Acknowledgments

The author gratefully acknowledges the comments from Professors Meneveau and Ohkitani, which help improve significantly the paper.

- 
- [1] H. K. Moffatt. The degree of knottedness of tangled vortex lines. *J. Fluid Mech.*, 35:117–129, 1969.
  - [2] R. Betchov. Semi-isotropic turbulence and helicoidal flows. *Phys. Fluids*, 4(7):925–926, 1961.
  - [3] J. J. Moreau. Constants d’un ilot tourbillonnaire en fluide parfait barotrope. *C. R. Acad. Sci. Paris*, 252:2810, 1961.
  - [4] R. B. Pelz, L. Shtilman, and A. Tsinober. The helical nature of unforced turbulent flows. *Physics of Fluids*, 29(11):3506–3508, 1986.
  - [5] C. G. Speziale. On helicity fluctuations and the energy cascade in turbulence. *Recent Advances in Engineering Science, Lecture Notes in Engineering*, edited by S. L. Koh and C. G. Speziale (Springer-Verlag, Berlin, 1989), 39:50, 1989.
  - [6] H. K. Moffatt. *Magnetic Field Generation in Electrically Conducting Fluids*. Cambridge University Press, 1978.

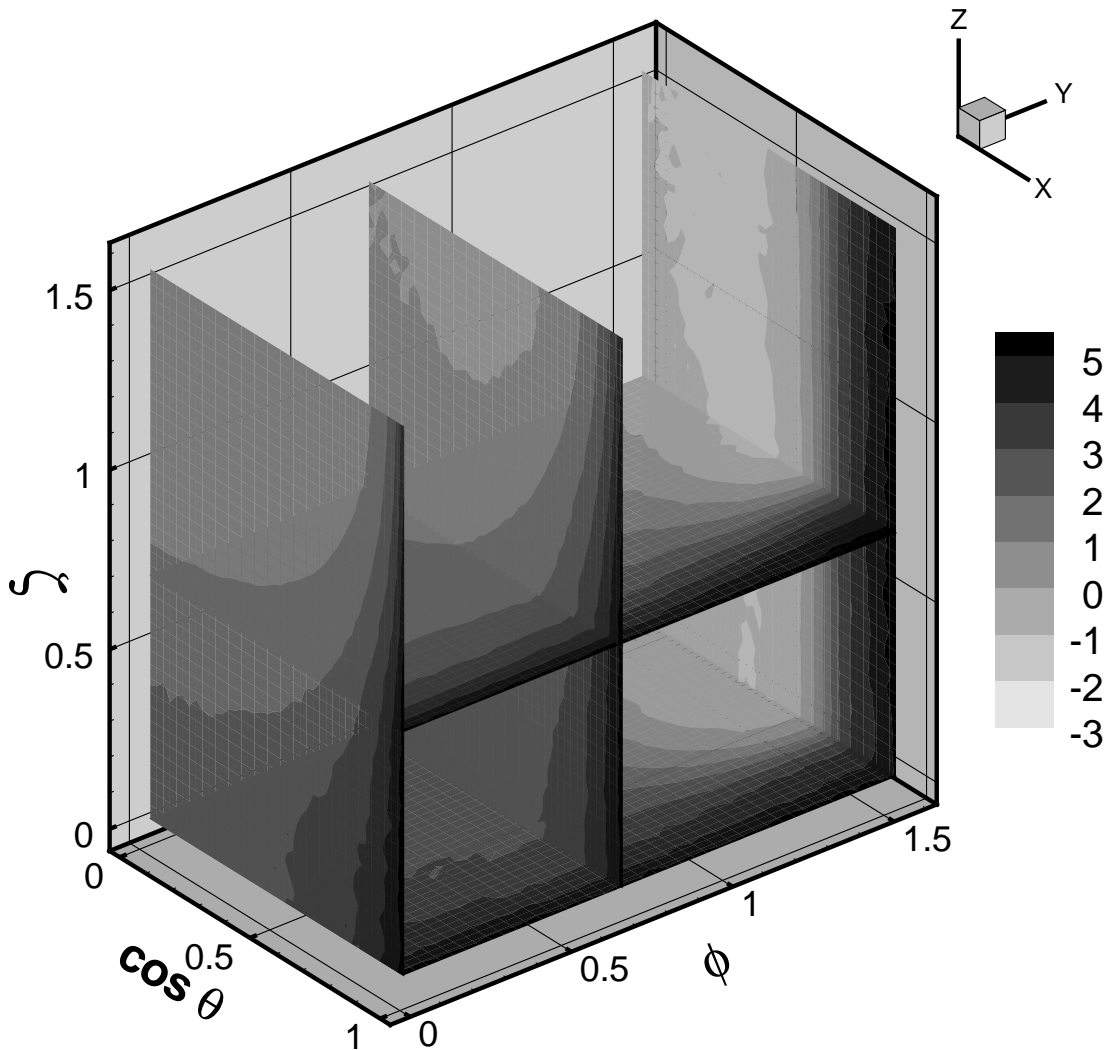


FIG. 34: Weighted averaged SGS helicity dissipation conditioned on  $(\cos \theta, \phi, \zeta)$ :  $P(\cos \theta, \phi, \zeta) \langle \Pi_H | \cos \theta, \phi, \zeta \rangle / \langle \Pi_H \rangle$ .

- [7] H. K. Moffatt. Magnetostatic equilibria and analogous Euler flows of arbitrarily complex topology. I. Fundamentals. *J. Fluid Mech.*, 159:359, 1985.
- [8] A. Brissaud, U. Frisch, J. Leorat, M. Lesieur, and A. Mazure. Helicity cascades in fully developed isotropic turbulence. *Phys. Fluids*, 16:1366, 1973.
- [9] J. C. André and M. Lesieur. Influence of helicity on the evolution of isotropic turbulence at high Reynolds number. *J. Fluid Mech.*, 81:187, 1977.
- [10] V. Borue and S. A. Orszag. Spectra in helical three-dimensional homogeneous isotropic turbulence. *Phys. Rev. E*, 55:7005, 1997.

- [11] Q. Chen, S. Chen, and G. L. Eyink. The joint cascade of energy and helicity in three-dimensional turbulence. *Physics of Fluids*, 15(2):361–374, 2003.
- [12] R. M. Kerr. Histograms of helicity and strain in numerical turbulence. *Phys. Rev. Lett.*, 59:783, 1987.
- [13] T. Gomez, H. Politano, and A. Pouquet. Exact relationship for third-order structure functions in helical flows. *Phys. Rev. E*, 61(5):5321–5325, May 2000.
- [14] S. Kurien, M. A. Taylor, and T. Matsumoto. Isotropic third-order statistics in turbulence with helicity: the 2/15-law. *J. Fluid Mech.*, 515:87–97, 2004.
- [15] P. D. Mininni, A. Alexakis, and A. Pouquet. Large-scale flow effects, energy transfer, and self-similarity on turbulence. *Physical Review E (Statistical, Nonlinear, and Soft Matter Physics)*, 74(1):016303, 2006.
- [16] W. Polifke and L. Shtilman. The dynamics of helical decaying turbulence. *Phys. Fluids A*, 1:2025, 1989.
- [17] M. M. Rogers and P. Moin. Helicity fluctuations in incompressible turbulent flows. *Phys. Fluids*, 30:2662, 1987.
- [18] J. M. Wallace, J.-L. Balint, and L. Ong. An experimental study of helicity density in turbulent flows. *Phys. Fluids A*, 4:2013, 1992.
- [19] Q. Chen, S. Chen, G. L. Eyink, and D. D. Holm. Intermittency in the joint cascade of energy and helicity. *Phys. Rev. Lett.*, 90:214503, 2003.
- [20] Y. Choi, B. Kim, and C. Lee. Alignment of velocity and vorticity and the intermittent distribution of helicity in isotropic turbulence. *Phys. Rev. E*, 80(1):017301, 2009.
- [21] H. K. Moffatt and A. Tsinober. Helicity in laminar and turbulent flow. *Annu. Rev. Fluid Mech.*, 24:281, 1992.
- [22] D. K. Lilly. The structure, energetics and propagation of rotating convective storms, Part II: Helicity and storm stabilization. *J. Atmos. Sci.*, 43:126, 1986.
- [23] W.-S. Wu, D. K. Lilly, and R. M. Kerr. Helicity and thermal convection with shear. *J. Atmos. Sci.*, 49:1800, 1992.
- [24] P. D. Mininni and A. Pouquet. Helicity cascades in rotating turbulence. *Phys. Rev. E*, 79:026304, 2009.
- [25] D. D. Holm and R. Kerr. Transient vortex events in the initial value problem for turbulence. *Phys. Rev. Lett.*, 88:244501, 2002.
- [26] D. D. Holm and R. M. Kerr. Helicity in the formation of turbulence. *Phys. Fluids*, 19:025101, 2007.
- [27] D. Chae. Remarks on the helicity of the 3-d incompressible euler equations. *Commun. Math.*

- Phys.*, 240:501–507, 2003.
- [28] C. Foias, L. Hoang, and B. Nicolaenko. On the helicity in 3d-periodic Navier-Stokes equations i: the non-statistical case. *Proc. London Math. Soc.*, 94:53–90, 2007.
- [29] C. Foias, L. Hoang, and B. Nicolaenko. On the helicity in 3d-periodic Navier-Stokes equations ii: the statistical case. *Commun. Math. Phys.*, 290:679–717, 2009.
- [30] L. C. Berselli and D. Cordoba. On the regularity of the solutions to the 3d Navier-Stokes equations: a remark on the role of the helicity. *Comptes Rendus Mathematique*, 347(11-12):613–618, 2009.
- [31] G. L. Eyink. Multi-scale gradient expansion of the turbulent stress tensor. *J. Fluid Mech.*, 549:159–190, 2006.
- [32] C. Meneveau and J. Katz. Scale-invariance and turbulence models for large-eddy simulation. *Annu. Rev. Fluid Mech.*, 32:1–32, 2000.
- [33] B. Tao, J. Katz, and C. Meneveau. Statistical geometry of subgrid-scale stresses determined from holographic particle image velocimetry measurements. *J. Fluid Mech.*, 457:35–78, 2002.
- [34] K. Horiuti. Roles of non-aligned eigenvectors of strain-rate and subgrid-scale stress tensors in turbulence generation. *J. Fluid Mech.*, 491:65–100, 2003.
- [35] Wm. T. Ashurst, A. R. Kerstein, R. M. Kerr, and C. H. Gibson. Alignment of vorticity and scalar gradient with strain rate in simulated Navier-Stokes turbulence. *Phys. Fluids*, 30:2343–2353, 1987.
- [36] A. Tsinober, E. Kit, and T. Dracos. Experimental investigation of the field of velocity-gradients in turbulent flows. *J. Fluid Mech.*, 242:169–192, 1992.
- [37] B. J. Cantwell. Exact solution of a restricted Euler equation for the velocity gradient tensor. *Phys. Fluids A*, 4:782–793, 1992.
- [38] L. Shtilman, M. Spector, and A. Tsinober. On some kinematic versus dynamic properties of homogeneous turbulence. *J. Fluid Mech.*, 247:65–77, 1993.
- [39] A. Vincent and M. Meneguzzi. The dynamics of vortex tubes in homogeneous turbulence. *J. Fluid Mech.*, 258:245–254, 1994.
- [40] K. K. Nomura and G. K. Post. The structure and dynamics of vorticity and rate of strain in incompressible homogeneous turbulence. *J. Fluid Mech.*, 377:65–97, 1998.
- [41] A. Ooi, J. Martin, J. Soria, and M. S. Chong. A study of evolution and characteristics of the invariants of the velocity-gradient tensor in isotropic turbulence. *J. Fluid Mech.*, 381:141–174, 1999.
- [42] M. Guala, B. Lüthi, A. Liberzon, A. Tsinober, and W. Kinzelbach. On the evolution of material lines and vorticity in homogeneous turbulence. *J. Fluid Mech.*, 533:339–359, 2005.

- [43] B. Lüthi, A. Tsinober, and W. Kinzelbach. Lagrangian measurement of vorticity dynamics in turbulent flow. *J. Fluid Mech.*, 528:87–118, 2005.
- [44] G. Gulitski, M. Kholmyansky, W. Kinzelbach, B. Luethi, A. Tsinober, and S. Yorish. Velocity and temperature derivatives in high-Reynolds-number turbulent flows in the atmospheric surface layer. Part 3. Temperature and joint statistics of temperature and velocity derivatives. *J. Fluid Mech.*, 589:103–123, OCT 25 2007.
- [45] K. Ohkitani. Eigenvalue problems in three-dimensional Euler flows. *Phys. Fluids A*, 5:2570–2572, 1993.
- [46] P. Constantin. Geometric statistics in turbulence. *SIAM Rev.*, 36:73–98, 1994.
- [47] B. Galanti, J. D. Gibbon, and M. Heritage. Vorticity alignment results for the three-dimensional Euler and Navier-Stokes equations. *Nonlinearity*, 10:1675–1694, 1997.
- [48] S. Y. Chen, R. E. Ecke, G. L. Eyink, X. Wang, and Z. Xiao. Physical mechanism of the two-dimensional enstrophy cascade. *Phys. Rev. Lett.*, 91:214501, 2003.
- [49] P. Constantin and C. Fefferman. Direction of vorticity and the problem of global regularity of the navier-stokes equation. *Indiana Univ. Math. J.*, 42:775–789, 1993.
- [50] P. Constantin, I. Procaccia, and D. Segel. The creation and dynamics of vortex tubes in three-dimensional turbulence. *Phys. Rev. E*, 51:3207–3222, 1995.
- [51] B. Galanti, I. Procaccia, and D. Segel. Dynamics of vortex lines in turbulent flows. *Phys. Rev. E*, 54:5122–5133, 1997.
- [52] Y. Li, C. Meneveau, S. Chen, and G. L. Eyink. Subgrid-scale modeling of helicity and energy dissipation in helical turbulence. *Phys. Rev. E*, 74:026310, 2006.
- [53] H. S. Kang and C. Meneveau. Effect of large-scale coherent structures on subgrid-scale stress and strain-rate eigenvector alignments in turbulent shear flow. *Phys. Fluids*, 17:055103, 2005.
- [54] P. Vieillefosse. Local interaction between vorticity and shear in a perfect incompressible fluid. *J. Phys.*, 43:837–842, 1982.
- [55] A. E. Perry and M. S. Chong. A description of eddying motions and flow patterns using critical-point concepts. *Annu. Rev. Fluid Mech.*, 19:125–155, 1987.
- [56] J. Martin, C. Dopazo, and L. Valiño. Dynamics of velocity gradient invariants in turbulence: restricted Euler and linear diffusion models. *Phys. Fluids*, 10:2012–2025, 1998.
- [57] F. van der Bos, B. Tao, C. Meneveau, and J. Katz. Effects of small-scale turbulent motions on the filtered velocity gradient tensor as deduced from holographic particle image velocimetry measurements. *Phys. Fluids*, 14:2456–2474, 2002.
- [58] P. Vieillefosse. Internal motion of a small element of fluid in an inviscid flow. *Physica A*, 125:150–162, 1984.

- [59] S. B. Pope. *Turbulent flows*. Cambridge University Press, Cambridge, 2000.
- [60] R. Betchov. An inequality concerning the production of vorticity in isotropic turbulence. *J. Fluid Mech.*, 1:497–504, 1956.
- [61] T. S. Lund and M. M. Rogers. An improved measure of strain state probability in turbulent flows. *Phys. Fluids*, 6:1838–1847, 1994.
- [62] A. Vincent and M. Meneguzzi. The spatial structure and statistical properties of homogeneous turbulence. *J. Fluid Mech.*, 225:1–20, 1991.
- [63] K. Horiuti and Y. Takagi. Identification method for vortex sheet structures in turbulent flows. *Phys. Fluids*, 17:121703, 2005.